Hyperbranched polyethyleneimine towards the development of homogeneous and highly porous CuO-CeO_2-SiO_2 catalytic materials

Hyperbranched polyethyleneimine towards the development of homogeneous and highly porous CuO-CeO_2-SiO_2 catalytic materials

A. Papavasiliou[1*], D. Tsiourvas[1], E. G. Deze[1], S. K. Papageorgiou[1], F. K. Katsaros[1], E. Poulakis[2], C. J. Philippopoulos[2], N. Boukos[1], Q. Xin[3], P. Cool[3]

[1] Institute of Nanoscience and Nanotechnology (INN), National Center for Scientific Research "Demokritos", Aghia Paraskevi 153 10 Athens, Greece

[2] Chemical Process Engineering Laboratory, Department of Chemical Engineering, National Technical University of Athens, 9 Heroon Polytechniou Str., Zografou Campus, 157 80 Athens, Greece

[3]Laboratory of Adsorption and Catalysis, University of Antwerpen (CDE), Universiteitsplein 1, 2610 Wilrijk, Belgium

* Corresponding author. e-mail: a.papavasiliou@inn.demokritos.gr

Abstract

A novel templating strategy for the development of composite nanoporous $CuO/CeO_2/SiO_2$ materials with advanced properties and significant thermal stability is proposed in this work, for potential use in automotive catalysts. The synthetic process is based on the dual role of low cost hyperbranched polyethyleneimine (PEI) acting both as a reactive template to control the formation of a siliceous porous network and as a metal chelating agent to facilitate the incorporation of finely dispersed CuO/CeO_2 nanoparticles into the silica matrix. Direct Ce(III)/Cu(II) introduction into the reaction mixture or post-synthetic impregnation of a preformed hybrid organic/inorganic xerogel was employed. Materials properties were assessed by means of XRD, SEM, TEM, N_2 adsorption, TPR and XPS techniques. Final Cu loading was determined by a novel UV-Vis spectroscopic method. Activity tests were performed under stoichiometric, O_2-deficient and O_2-rich conditions simulating realistic exhaust environment. Catalytic performance was found to be strongly depended on the employed synthetic pathway. The $CuO/CeO_2/SiO_2$ composites prepared by direct introduction, exhibited enhanced structural characteristics (BET≈ 680 m^2/g), high homogeneity, superior oxidation performance and notable thermal stability, with great potential for use in automotive aftertreatment systems.

Keywords: TWCs; hyperbranched polymer; mesoporous silica; Ceria; Copper; thermal ageing.

1. Introduction

Emissions originating from automotive engines trigger serious ecological and health hazards, i.e. acid rain, smog formation, global warming, and ozone layer depletion. Given the implementation of ever stricter measures and directives towards lowering tail-pipe emission values [1-3], efficient control and suppression of combustion engines' harmful effluents is still considered a very challenging research objective in the field of environmental catalysis.

Nowadays, three way catalytic converters (TWCs) have been established as the most effective technology for vehicular emission abatement. Their operation relies on the transformation of the main exhaust gas pollutants such as CO, C_xH_y and NO_x to inactive CO_2, N_2 and H_2O [4-6]. Platinum group metals (PGMs), especially Pt, Pd and Rh, are considered key components for the simultaneous reduction and oxidation reactions carried out over the TWC. However scarcity and relatively high price of PGMs, render their reduction or even their replacement mandatory [6-7].

In an attempt to develop low cost catalytic systems, research efforts have been directed towards the exploitation of transition metals serving as the catalytic active phase [8-15]. A considerable number of studies have been dealing with copper–based catalysts, concerning oxidation reactions, e.g. oxidation of CO and HCs, preferential oxidation of CO (CO-PROX), soot oxidation, as well as selective catalytic reduction of NO and water-gas shift reaction [8-15]. Recently, a combination of PGM-based alumina catalyst and copper supported on a mixed cerium oxide carrier has been reported to achieve advanced performance at a very low temperature range [16].

Cerium oxide constitutes an essential promoter widely used in TWCs. In general, it acts as oxygen storage component, support stabilizer and auxiliary catalytic material, favoring the water-gas shift reaction (WGS), CO oxidation and steam reforming

reactions. In addition, through metal-support interactions, it enhances metal dispersion and catalytic activity at the interfacial sites [4-5, 17]. Its beneficial role emanates from its ability to undergo rapid redox cycles associated with the facile generation and refilling of oxygen vacancies [18]. Catalytic systems comprising of CuO/CeO_2 have gained considerable interest as noble metal-free alternatives with synergetic redox properties at the CuO/CeO_2 interfacial positions being responsible for their high catalytic activity [19-21]. However, ceria possess very poor thermal stability and it is prone to crystal growth upon thermal treatment [4]. Ceria's nanometer scale particle size is of primary importance, since it provides a larger number of anionic vacancies and active surface oxygen species enhancing its oxygen storage capacity (OSC) and catalytic activity [4-5].

The adopted synthetic strategy is another very crucial factor influencing the overall catalytic performance since it determines the particle size and deposition of the active phase [4]. In general, the most common approaches reported, involve impregnation of oxide supports with aqueous solutions of metal salts, combustion, co-precipitation and sol-gel routes [12-13, 16, 19]. Lately, great efforts towards the production of CuO-CeO_2 materials with enhanced textural properties have led to the design of nanostructured Cu–Ce–O materials as well as the utilization of mesoporous supports, mostly SBA-15, as hosts for the inclusion of active species [11, 14, 17, 22-31]. Gu et al. [28] and Zabilskiy et al [29] described the synthesis of ordered mesoporous Cu–Ce–O catalysts with surface areas around 159 m^2g^{-1} by nanocasting with mesoporous silica (KIT-6) as a sacrificial template. Mesoporous nanostructured $CuO/Ce_{0.8}Zr_{0.2}O_2$ catalysts, very active for low-temperature CO oxidation, have been prepared by the surfactant-assisted method of nanoparticle assembly [24]. Moretti et al. [22] have produced a Cu-Ce-Al-based mesoporous material of high surface area (>400 m^2g^{-1})

through a single step synthetic approach employing metal stearates both as Cu-Ce sources and structural directing agents and tested it in the CO-PROX reaction. In spite of the large surface areas attained, soft templating routes often yield composite Cu–Ce–O materials with poor thermal durability, suffering severe porous structure deterioration or even collapse when subjected to thermal treatment above 600 ^{o}C. Hard templating methods, although more effective in producing stable structures, require complicated synthetic protocols including time-consuming procedures for the preparation of hard templates and post-synthesis treatments with NaOH or HF solution to remove the siliceous matrix.

On the other hand, using nanoporous solids for the preparation of supported CuO-CeO_2 systems could prove a very efficient pathway towards stable materials with increased surface areas, pore volumes, nanosized and well-dispersed CuO and ceria particles. In our previous work hyperbranched polyethyleneimine (PEI), an inexpensive polymer readily available in bulk quantities and in several molecular weights [32-33], was successfully employed as a reactive template, for the synthesis of nanoporous silica with tailored porosity [32]. However, its presence into the siliceous matrix could offer an additional advantage. The large number of its functional amino groups and its property to chelate a wide variety of metal ions, including copper and lanthanides [34-40], can make it a vehicle for the incorporation of guest metal species into the siliceous framework in an easy and controlled manner.

In this work, based on this dual action of PEI, composite nanoporous $CuO/CeO_2/SiO_2$ with advanced properties and significant thermal stability were developed, for potential use in automotive catalysts. Such materials, to the best of our knowledge, have never been evaluated under real exhaust environment. The prepared materials were evaluated under simulated exhaust conditions using stoichiometric,

fuel-rich and fuel-lean mixtures. A thorough investigation of structural, morphological, chemical and redox properties was carried out by means of UV-Vis, XRD, N_2 adsorption, SEM, TEM, TPR and XPS analyses. In order to assess thermal stability, the sample with the optimum catalytic performance was subjected to an aging procedure.

2. Experimental

2.1. Materials

Hyperbranched polyethyleneimines with molecular weights of 5.000 Da (Lupasol® G100) and 25.000 Da (Lupasol® WF), kindly donated by BASF (Ludwigshafen, Germany), were extensively dried under vacuum before use. The primary:secondary:tertiary amino groups ratios of PEI5 (1:1.10:0.96) and PEI25 (1:1.18:1) were determined by inverse gated 13C NMR. 3-(Triethoxysilyl)propyl isocyanate, (TESPI, 95%, Aldrich), Cerium(III) nitrate hexahydrate, $Ce(NO_3)_3 \cdot 6H_2O$, (99%, Aldrich), Copper(II) nitrate trihydrate, $Cu(NO_3)_2 \cdot 3H_2O$ (99%, Acros Organics Chemicals) and $CuCl_2 \cdot 2H_2O$ (≥99.0%, Aldrich) serving as silica's, ceria's and copper's precursors were used as received. N,N-Dimethylformamide (DMF, 99.8%) supplied from Sigma–Aldrich was dried over molecular sieves.

2.2 Catalytic Materials preparation

Pure nanoporous silica's synthetic pathway, which is described in our previous work [32], involved dissolution of PEI (M_w=5000, BASF) in DMF under argon atmosphere (PEI:DMF weight ratio was 1:9). Then 3-(triethoxysilyl)propyl isocyanate (TESPI) was added drop-wise, while the solution was kept at 0 ^oC for one hour, followed by stirring for 24 h at RT. The molar ratio of TESPI added with respect to

the reactive primary and secondary amino groups of PEI was 20 %. During the 24 h stirring, interaction between the terminal amino groups of hyperbranched polyethyleneimine and the isocyanate group of silica's precursor is taking place and triethoxysilyl hyperbranched polymers are obtained. The reaction was performed under anhydrous conditions to prevent hydrolysis of the isocyanate and ethoxysilane groups. Subsequently, complete hydrolysis and silanol formation was attained by allowing the triethoxysilyl derivatives in open air for 96 h. Then, the reaction vessel was placed in an oven at 90 ^{o}C for 50 h for complete siloxane bridge formation. Finally, the organic part was removed by calcination in a tube furnace at 700 ^{o}C for 2 h under airflow at a heating rate of 2 ^{o}C/min.

The same synthetic route was employed for the production of the mixed silica – ceria support. Cerium nitrate ($Ce(NO_3)_3 \cdot 6H_2O$), which was used as the ceria precursor, was dissolved in a small amount of DMF and added drop-wise into the reaction mixture, 24 h after the introduction of TESPI. The Si:Ce molar ratio was set to 11.5 so as to get a final composite material comprised of 80 wt % SiO_2 and 20 wt % CeO_2. Under these conditions the molar ratio of Ce ions to the primary amino groups of PEI was Ce:N = 1:28.

Copper introduction was attained either during nanoporous silica or silica-ceria xerogel synthesis (one – step synthesis) or by post-synthesis impregnation of the hybrid organic/inorganic material into $CuCl_2 \cdot 2H_2O$/acetone solution (two – step synthesis). In the one – step synthesis, copper nitrate ($Cu(NO_3)_2 \cdot 3H_2O$) was dissolved in DMF and introduced into the reaction mixture 5 h after the addition of cerium nitrate. The amounts of cerium and copper precursors added were calculated so as to obtain solids with 20 wt % CeO_2 and 2 or 6.5 wt % Cu, which correspond to Ce:N ratio of 1:28 and Cu:N ratios of 1:105 or 1:32, respectively. In the two-step synthesis,

hybrid SiO_2/PEI and SiO_2-CeO_2/PEI xerogels, obtained after complete siloxane bridge formation, were immersed into $CuCl_2 \cdot 2H_2O$ acetone solution of 1000 ppm initial Cu concentration. After 24 h in a shaking bath (150 rpm, RT), the impregnated solids were collected and thoroughly washed with an excess of acetone to remove any uncomplexed Cu(II). All samples were dried at 35 ^oC and calcined in a tube furnace at 700 ^oC under airflow in order to remove the organic template.

Samples' coding, final chemical composition and synthesis conditions are summarized in Table 1. In an attempt to evaluate materials' thermal stability an additional sintering procedure was employed. Portion of the fresh material (calcined at 700 ^oC) with the optimum catalytic behavior was aged at 800 ^oC for 5 h in air.

2.3 Characterization techniques

2.3.1 PEI-Ce(III) and PEI-Cu(II) complex formation

Complex formation of Cu(II) or Ce(III) with PEI was studied by means of UV-Vis spectroscopy, employing a Cary 100 Conc UV-Visible spectrophotometer. The corresponding spectra were obtained after the addition of increasing quantities of $Ce(NO_3)_3 \cdot 6H_2O$ or $Cu(NO_3)_2 \cdot 3H_2O$ in a PEI 10% solution in dry DMF and up to a to metal ion:N molar ratio of 1:4. For comparison purposes the complex formation of Cu(II) with PEI in water was also followed under the same conditions. All DMF solutions used in this work were extensively dried and degassed.

2.3.2 Determination of copper content

The concentration of copper in the final products was determined by UV-Vis spectroscopy, after complete solubilization of the inorganic matrices, employing a Cary 100 Conc UV-Visible spectrophotometer (Varian Inc., Mulgrave, Victoria,

Australia) in the wavelength range of 300–900 nm. The methodology involves a two-step digestion procedure in order to convert both the silica matrix and the copper oxide particles into water soluble species. In the first step, a specific amount of solid sample (around 0.1g) was dispersed in 10 mL of 0.5 N NaOH, placed in a tightly closed Teflon digestion vessel and kept at 95 ^{o}C for 1h under static conditions. After reaching room temperature, the partially dissolved mixture was acidified with 3 mL of 6 N HCl (pH <3.0) and placed in a bath sonicator for 30 min at 40 ^{o}C. Following the complete dissolution of the sample, a small portion (2.5 mL) was collected and 0.7 mL of 2N NaOH and 0.4 mL of a 20 wt% aqueous solution of polyethyleneimine with molecular weight of 25.000 Da (PEI25K) were added consecutively. The intermediate addition of NaOH before the addition of PEI25K, is necessary to avoid any possible oxidation of polyethyleneimine likely to occur in the strongly acidic environment (pH <3.0). The formation of PEI25K – copper complexes, evidenced by the emergence of a deep blue color, is taking place within seconds. Finally, the pH of the solution was adjusted at pH=10.0±0.1 with the addition of appropriate quantities of 2N NaOH (typically 0.7 mL) and the determination of Cu content was carried out by registering its optical density at 645 nm. A calibration curve was also constructed by registering the optical density at 645 nm of a series of standard solutions of copper(II) chloride treated as above with consecutive additions of 0.5N HCl (2.5 mL), 2N NaOH (0.7 mL), and 20 wt% PEI25K (0.4 mL) and final adjustment of the pH of each solution at 10.0±0.1. Thus, a linear calibration curve (R^2=0.99772) was obtained over the concentration range 20 - 200 ppm.

2.3.3 Powder X-ray diffraction

Low and wide angle XRD diffraction patterns were acquired using a Rigaku rotating anode X-ray generator (operating at 50 kV, 100 mA, nickel-filtered CuKa1 radiation) and an R-AXIS IV imaging plate. Samples were sealed in Lindemann capillaries.

2.3.4 N_2 adsorption analysis

N_2 adsorption isotherms were collected at 77 K on an automated volumetric system (AUTOSORB-1-Krypton version – Quantachrome Instruments). Prior to the measurements the samples were outgassed under vacuum at 250 °C for 24 h. Specific surface area was determined using the Brunauer– Emmett–Teller (BET) method. The pore size distribution was calculated using the Nonlocal Density Functional Theory (NLDFT) model (Quantachrome Instruments, AS1Win, v. 2.01, DFT software). Data reduction parameters: Calc. Model: N_2 at 77 K on silica (cylindrical pore, NLDFT equilibrium model).

2.3.5 Scanning Electron Microscopy

Samples' morphological investigation was conducted with a Jeol JSM 7401F Field Emission Scanning Electron Microscope equipped with Gentle Beam mode. The applied acceleration voltage was 2 kV and samples were mounted on metallic (brass) substrates using a double coated carbon conductive tape.

2.3.6 Transmission Electron Microscopy

The morphology and crystallinity of the samples in the nanoscale was examined utilizing an FEI CM20 TEM equipped with a Gatan GIF 200 Energy Filter for electron energy loss elemental mapping. Electron Energy Loss Spectroscopy (EELS)

has been utilized to study the dispersion of Ce and Cu in the SiO_2 nanoporous matrix. Energy Filtered TEM (EFTEM) images were obtained , using the EELS Ce M-edge at 883eV and Cu M-edge at 74eV energy loss and applying the three window method [41] as incorporated in Gatan Digital Micrograph software. It should be mentioned that the low loss Cu M-edge was used, instead of the usual Cu L-edge at 931eV, since the tail of the Ce M-edge at 883eV extends over the Cu L-edge making the three window method inapplicable.

2.2.7 Temperature programmed reduction

Temperature programmed reduction measurements of the catalysts were performed in a Quantachrome iQ. About 50 mg of the sample were outgassed at 473 K for 16 h. After cooling, the sample was first pretreated at 523 K under a He flow for 1 h. Consequently the samples were reduced with 5 % H_2/Ar at a flow rate of 25 mL/min and the temperature was increased from 313 K to 1073 K at 10 K/min. The hydrogen consumption was continuously monitored using a thermal conductivity detector (TCD).

2.2.8 XPS

The photoemission experiments were carried out in an ultra-high vacuum system (UHV) which consists of a fast entry specimen assembly, a sample preparation and an analysis chamber. The base pressure in both chambers was $1\times10{-}9$ mbar. Unmonochromatized AlKα line at 1486.6 eV and an analyzer pass energy of 97 eV, giving a full width at half maximum (FWHM) of 1.7 eV for the Au 4f7/2 peak, were used in all XPS measurements. The XPS core level spectra were analysed using a fitting routine, which can decompose each spectrum into individual mixed Gaussian-

Lorentzian peaks after a Shirley background subtraction. The measurement errors for the XPS core level peaks positions are about ±0.05 eV. Calibration of the analyser's kinetic energy scale was performed according to ASTM-E 902-88. Apart from the Wide Scan, core level peaks that were recorded were: C1s, O1s, Ce3d, and Cu2p.

2.2.9 Catalytic activity measurements

The apparatus used for the activity tests is illustrated in Fig. S1. Catalytic samples (200 mg) were placed in the middle of a stainless steel tube reactor of 7mm inner diameter. Quartz wool was added at both sides of the catalyst to stabilize its position inside the reactor. The reactor was fitted inside a temperature controlled furnace and the catalyst temperature was continuously monitored by two thermocouples situated on the outer side of the reactor before and after the catalyst. In an effort to better simulate real exhaust conditions, the experimental protocol followed for the acquisition of activity measurements involves a complex feed stream containing 10 % H_2O, CO_2 and a mixture of hydrocarbons (CH_4, C_3H_8 and C_3H_6). The gas mixture feed was prepared from the following six gas cylinders: 2000ppm NO and N_2 (balance), air, N_2, CO, and a mixture of 0.15% CH_4, 0.15% C_3H_8, 0.28% C_3H_6, 1.59% H_2 and N_2 (balance). The volumetric flow of each stream was controlled by thermal mass flows (Brooks Instrument) and a total feed similar to the typical composition of car exhaust gases in lean, stoichiometric and rich conditions (λ=0.98, λ=1, λ=1.08) was prepared, as shown in table 2. The total volumetric flow was set to 200 Nml/min in order to correspond to 60000h^{-1} space velocity. The addition of 10% H_2O was obtained by passing the feed through a thermo stated water bubbler. In the outlet stream, hydrocarbon concentrations were monitored by gas chromatography (Shimadzu GCe17A, column HP PlotQ, FID detector), NO/ NO_2 concentrations by a

chemiluminescence analyzer (Model 42-HL, Thermo Scientific) and CO concentration by an electrochemical detector (Dräger X-am® 7000).

To ensure stable operation of the catalytic materials before the evaluation of the catalytic activity, samples were treated with gas feed in stoichiometric composition (50 Nml/min total volumetric rate). The temperature ramp was set to 20 – 500^{o}C with 8^{o}C/min rate and remained at 500^{o}C for 2 hrs. The activity tests were performed between 50 to 500^{o}C and conversion performance was recorded every 50^{o}C.

3. Results and Discussion

3.1 Synthesis strategy

In our previous work the successful imprinting of nanoporous cavities into silica structure was demonstrated by employing hyperbranched polyethyleneimine as a reactive template [32]. The synthetic strategy relied on the preparation of silylated PEI networks through the reaction of primary and secondary amino groups of PEI with the isocyanate group of silica's precursor. The formation of triethoxysilyl functionalized macromolecules and the subsequent cross-linking through hydrolysis and polycondensation reactions were confirmed by FTIR spectroscopy through the detection of the amide bands, Si–OH groups and Si–O–Si bonds respectively [32]. Thermal treatment at elevated temperature effectively removed the organic template and led to the formation of a novel silica network architecture. Driven by this study and taking advantage of the well-known chemical and chelating properties of PEI [33-40], integrated into the hybrid matrix before calcination, we have employed this novel templating procedure for the easy and inexpensive production of homogeneous composite nanostructured oxides. The synthetic protocol involves a Si:PEI molar ratio of 20 %, DMF as solvent and PEI of 5000 Da molecular weight. The Si:PEI molar

ratio employed remains low in order to have a considerable amount of amino groups (80%) available for subsequent complexation with Ce and Cu ions, while the metal ions:N ratio employed is also considerably lower than the maximum complexation ability of PEI under the experimental conditions employed (see section 3.2 below). As shown in Table 1, samples were produced with a view to investigate the effects of chemical composition, direct or post synthetic copper species inclusion and copper content.

3.2 Formation of PEI-CeIII & PEI-CuII complexes

The formation of Cu and Ce complexes with PEI in DMF under the conditions employed is established in separate experiments using UV-Vis spectroscopy. It is well documented [34-36] that PEI forms copper chelates in water, typically with a Cu:N molar ratio of about 1:5. The chelate has the dark blue cuprammonium color and a large equilibrium constant (at Cu:N ratio of 1:5, about 96% of the reactants are in the form of the chelate). The complexes are highly water soluble and obey Lambert and Beer Laws with molar extinction coefficients, ε, of about 175 $M^{-1}cm^{-1}$ at 635 nm and of 425 $M^{-1}cm^{-1}$ at 270 nm (literature values depend both on solutions pH and PEI branched structure variations) [36]. Thus, complex formation can be followed by monitoring the absorbance of a PEI solution at 635 nm (PEI and uncomplexed Cu(II) absorption at this wavelength is negligible) upon addition of increasing amounts of Cu(II). In the region of PEI excess, the absorbance is linearly dependent on the Cu:N ratio, denoting quantitative formation of the chelate, while in the region of Cu(II) excess, the curve is a line of constant optical density [36]. In the intermediate region the absorbance deviates from the straight line suggesting incomplete complex formation and the presence of uncomplexed Cu(II).

In this study, PEI-Cu(II) complex formation in DMF, is indicated, upon mixing, by the formation of the intense blue cuprammonium color. Quantitative formation of the chelate is monitored by UV-Vis spectroscopy. Fig. 1A shows the absorbance of PEI and Cu(II) solutions and their complex in dry DMF (PEI concentration 10% w/w, RT), while in Fig. 1B the absorbance at λ_{max}=640 nm is plotted vs. increasing metal ion concentration. The observed linearity indicates quantitative complex formation up to 1:6 Cu:N ratio, considerably higher than the ratios used in this study (1:105 or 1:32). Moreover, given that both the absorbance curve and the extinction coefficient ε=140 $M^{-1}cm^{-1}$ obtained in DMF are very close to those of the aqueous PEI-Cu(II) complex under the same experimental conditions (λ_{max}=640 nm, ε=155 $M^{-1}cm^{-1}$, PEI concentration in water 10% w/w, rt), it is reasonable to suggest that in DMF complex structure is similar to that in water [34-36].

Neither PEI nor low molecular amines complex formation with Ce ions has been reported in the literature. The lack of N-coordinated complexes of the rare-earths in water was ascribed partly to the fact that nitrogen-donating ligands would form less stable complexes with these elements, and also to the fact that such ligands, being basic in nature, would precipitate hydroxides of these metals from their solutions [37]. However, formation of ethylenediamine, diethylenetriamine and triaminotriethylamine chelates of the tripositive lanthanide ions in a non-aqueous dry solvent, i.e. acetonitrile, have been reported in the literature [38-39]. Calorimetric measurement of the enthalpies of complexation of ethylenediamine with lanthanide ions in acetonitrile proved the considerable thermodynamic stability of lanthanide complexes based solely upon nitrogen coordination [40]. PEI complexation with Ce(III) in dry DMF is taking place as indicated by the appearance of a bright yellowish brown colour and monitored through the increase in absorbance in the

visible and near UV region with increasing metal ion concentration. If traces of water are present in DMF, the instantaneous formation of off-white precipitate, most likely cerium hydroxides, is observed. Fig. 2A shows that while the absorbance of PEI and Ce(III) solutions in DMF is negligible throughout the spectral range, their complex formed in DMF (PEI concentration in dry DMF 10% w/w, RT) exhibits a distinctly different spectrum with quite high extinction coefficient (ε=1440 M^{-1} cm^{-1} at 350 nm). In Fig. 2B the absorbance of PEI-Ce(III) complex at 350 nm (dilution 1:10), is plotted vs. increasing metal ion concentration. Again the acquired linearity suggests quantitative complex formation up to Ce:N ratio of 1:8, while significant deviation from the straight line is observed at higher ratios. It is therefore evident that PEI - Ce(III) complexes have indeed smaller equilibrium constants than their Cu counterparts, as suggested in the literature, however, for the Ce:N ratios used throughout our experiments (Ce:N = 1:28), it is reasonable to assume that quantitative complexation of Ce is attained.

3.3 Determination of copper content in the calcined samples

In order to determine the final copper content in the Cu and Ce loaded silica samples, a novel and straightforward procedure was developed based on the formation, at elevated pHs (with an optimum pH range of 9.8-10.1), of PEI-Cu(II) complexes having an intense blue colour. The protocol for Cu analysis includes sample digestion, Cu(II) complexation with PEI (PEI25K, Mw=25000) and UV-Vis spectrophotometrical determination. The presence of Ce ions does not interfere with the measurements since PEI does not form complexes with either Ce(III) or Ce(IV) in water, as it was previously stated. The reliability of the proposed procedure was

validated by atomic adsorption spectroscopy (AAS) as well as electron probe microanalyzer (EPMA). Cu content in the final solids ranges from 2 to 6.5 (Table 1).

3.4 X-ray diffraction analysis

All calcined materials exhibit a single broad 2θ reflection at the low – angle region between 0.9-2.6^{o}. Higher order Bragg reflections couldn't be resolved in any of the patterns, suggesting the successful formation of porous networks possessing, however, only short-range order in the pore arrangement. Broadness and symmetry of the low-angle diffraction peak changed upon Cu introduction. Interestingly, copper loaded materials display sharper, narrower and more uniform peaks compared to the parent samples, suggesting a higher degree of pore structure ordering (Fig. 3) in agreement with N_2 adsorption analysis, discussed in the following section. The respective FWHM values along with the coherent distances corresponding to the 2θ angles are listed in Table 3.

Wide angle X-ray diffraction patterns are depicted in Fig. 4. All diffractograms exhibit a very broad and low intensity peak at 2θ 20–30^{o}, typical of the amorphous character of the silicate pore walls. Diffraction peaks associated with the cubic fluorite structure of CeO_2 can also be distinguished at 2θ = 28.6^{o}, 33.1^{o} and 47.5^{o} (JCPDS No 34-0394). Their low intensity and broadness implies the nanocrystalline nature of ceria particles and the high homogeneity of the composite support with finely dispersed ceria nanoclusters. Detectable reflections characteristic of CuO crystal phase are present only in samples with high copper loading, whereas absence of these peaks in samples with low loading indicates highly dispersed copper species. Sharp and high intensity peaks ascribed to CuO crystal phase (tenorite phase, JCPDS No 48-1548) are identified only in $NSCu_{imp}$ and $NSCeCu_H$ samples with 6.5 wt % Cu

content. A rough estimate of CeO_2 and CuO particle sizes by using the Scherrer formula for CuO (111) and CeO_2 (111) reflections (Table 3), indicates the effect of the employed synthetic procedure on the final material's structural properties. In the sample derived from two-step synthesis ceria average size was found 5.3 nm, almost double to that of the one-step synthesis sample.

XRD investigation of the thermally aged sample ($NSCeCu_L$-aged) in the wide diffraction area revealed no signals assigned to CuO crystal phase and a negligible increase of ceria particle size, as determined by Scherrer formula (Fig. 4). Moreover, a well-resolved reflection emerged in the low angle region pointing out the preservation of the porous network (Fig. S2). This peak is narrower than the respective of the fresh sample, again in line with N_2 adsorption analysis. These results demonstrate the material is considerably stable after thermal treatment at an elevated temperature for a longer period (800 ^oC for 5 h).

3.5 N_2 adsorption analysis

N_2 adsorption analysis was employed in order to gain insight into the architecture of the formed porous networks. N_2 adsorption – desorption isotherms, illustrated in Fig. 5A, are characterized by a very steep initial uptake at low P/P_0 signifying a strong contribution of micropores followed by a gradually increasing adsorption branch related to the presence of mesoporosity. These isotherm plots could be classified between type I and IV and reflect the complex texture of the samples consisting of both micropores and mesopores.

Significant differences in terms of pore structural characteristics can be spotted among the catalytic materials. In the case of copper free samples (NS and NSCe) a deep microporous texture is observed. For the pure silica sample a super-microporous

nature is manifested by the type I isotherm plot featuring a rounded shaped knee indicative of supermicropores filling [42]. In mixed silica – ceria sample, the smooth inflection in the intermediate P/P_0 region is associated with the existence of complementary mesopores. On the other hand, Cu loaded solids demonstrate a more pronounced mesoporous character. This is evidenced by the stronger uptake in the 0.2 -0.5 P/P_0 region, characteristic of capillary condensation within mesopores, and the detection of a distinct hysteresis loop which is absent in the case of copper-free materials (Fig. 5A).

Pore size distribution analysis through the NLDFT treatment further supports the N_2 sorption isotherms findings (Fig. 5C). In the parent Cu free materials a bimodal PSD is obtained with peaks both in the micropore and mesopore area. On the contrary, in copper loaded materials a narrower monomodal PSD curve can be observed with a clear shift to higher pore diameters, confirming the prevalence of mesoporosity.

Table 4 summarizes the textural characteristics of the as-developed materials. The observed trend is a specific surface area decrease upon copper introduction accompanied by pore volumes of the same order or even larger than the respective of the parent nanoporous silicas (e.g. $NSCu_{imp}$ vs NS sample). This is attributed to the larger pore size of Cu loaded samples. In general, it can be deduced that metal incorporation into the siliceous matrix, regardless of the employed synthetic pathway, exerts a significant effect on material's pore geometry generating a larger mesopore fraction. This behavior could be related to the arrangement of the anchored copper ions inside the dendritic molecule leading to a reconfiguration of the hybrid organic-inorganic network.

As expected, in the thermally aged $NSCeCu_L$ sample, a 28 % reduction in specific surface area and a 24 % reduction in total pore volume were attained. However, the nanoporous structure was retained to a great extent as revealed by the unchanged shape of both N_2 sorption isotherm and PSD curve (Figs. 5B and 5D).

3.6 Scanning and Transmission Electron Microscopies

Micrographs obtained by SEM analysis depict the nanoporous solids' morphological characteristics. As shown in Figs. S3-4 (Supporting Information), all materials exhibit a homogeneous morphology, consisting of highly dense monolithic pieces. SEM micrographs of the copper loaded samples demonstrate the retention of morphological characteristics after metal introduction. However, closer inspection of materials' surface reveals a different texture among the samples. The smooth surface of copper free samples becomes rougher after copper loading. In addition, surface nanoporosity can be more easily detected in copper loaded samples, especially in $NSCeCu_H$ sample (Fig. S4C-D), confirming the results derived from the aforementioned analyses.

In-depth investigation of samples' homogeneity and nanoporous nature is provided by TEM examination. TEM micrographs of $NSCeCu_{imp}$, $NSCeCu_L$, $NSCeCu_H$ and $NSCeCu_L$-aged samples (Figs. 6-7) reveal a three-dimensional wormhole-like pore structure lacking long-range pore ordering as also indicated by low-angle XRD analysis. The porous network walls are semi-crystalline comprising of an amorphous silica phase with highly dispersed nanosized CeO_2 and CuO crystallite particles. High-resolution TEM images, illustrated in Figs. 6-7, shows the (111) with d=0.311nm and (110) with d=0.275nm lattice fringes of a CeO_2 and a CuO nanocrystal embedded in silica's amorphous matrix respectively. Although all the

examined samples are highly homogeneous, differences in distribution and particle size of CeO_2 and CuO guest species can be noticed. In Figs. 8C-D and 8E-F, Ce and Cu elemental maps of $NSCeCu_L$ and $NSCeCu_{imp}$ samples are presented, whereas their corresponding bright field images are shown in Figs. 8A-B. The intensity of the maps corresponds to the concentration of Ce (green) and Cu (red) in the nanoporous matrix. Clearly, $NSCeCu_L$ sample is the most homogeneous material containing the smallest CeO_2 crystallites of average size around 3 to 4 nm, in good agreement with the corresponding XRD data, and a remarkable dispersion of Cu species covering uniformly the siliceous material, as demonstrated in Fig. 8E. $NSCeCu_{imp}$ derived from a two-step synthetic pathway exhibits a lesser homogeneity degree, a poorer Cu dispersion (Fig. 8F) and larger CeO_2 and CuO crystallites compared to $NSCeCu_L$; whereas in $NSCeCu_H$ sample, with the highest Cu loading, the largest CeO_2 and CuO particles, reaching up to 30 – 35 nm, could be detected (Fig. 7). Finally, as revealed in Fig. 6C, the intriguing structural and morphological features of $NSCeCu_L$ sample are observed even after thermal aging at 800 ^oC, reflecting its significant thermal stability.

3.7 H_2-TPR study

H_2-TPR experiments were applied to investigate sample's redox behavior and the respective TPR profiles are illustrated in Fig. 9. $NSCu_{imp}$ sample demonstrates a complex TPR profile with overlapping reduction peaks, indicating the presence of several copper species with different dispersion degree. The small reduction peak centered at 300 ^oC can be related to copper oxide clusters highly dispersed onto the silica support [14, 22]. The main peak located at higher temperature around 400 ^oC can be decomposed into two contributions assigned to large CuO particles and isolated Cu^{2+} species. For the latter component a stepwise reduction mechanism is

reported in the literature [43], associated with the reduction of Cu^{2+} species to Cu^{1+} and Cu^{1+} to Cu^{0} which explains the small shoulder emerging at very high temperatures (≈ 560 ^{o}C).

In $NSCeCu_{imp}$, $NSCeCu_{L}$, $NSCeCu_{H}$ and $NSCeCu_{L}$-aged samples, shifting of reduction peaks to lower temperatures implies the generation of more reducible species due to synergistic effects between the ceria and copper active components [25, 44-46]. The temperatures where reduction of CuO initiates decreases with increasing copper loading, with simultaneous increase of peak area at higher temperatures (sample $NSCeCu_{H}$). Specifically, the maximum at 300 ^{o}C, detected in $NSCeCu_{imp}$ and $NSCeCu_{H}$ samples, is ascribed to small-sized highly dispersed copper oxide species mostly in contact with silica support. Reduction peaks below 300 ^{o}C can be attributed to Cu species strongly interacting with ceria and above 300 ^{o}C to larger CuO particles not in contact with ceria (as was observed for $NSCu_{imp}$ sample), as well as to ceria reduction [22]. The sharp high temperature peak at 330 ^{o}C spotted in $NSCeCu_{H}$ sample is in agreement with XRD analysis which revealed the presence of CuO in crystalline form. However, this peak's area and position compared to the respective of $NSCu_{imp}$ sample, containing only copper, reflects a lower amount and a smaller size of crystalline CuO. The optimum reduction behavior is obtained by $NSCeCu_{L}$ sample which exhibits the lowest temperature profile as a consequence of its high homogeneity, excellent Cu dispersion and small CeO_2 nanoparticles. Moreover, this sample preserves its redox properties even after thermal aging, as evidenced by the unchanged TPR profile.

3.8 XPS study

XPS measurements were performed in an effort to elucidate the surface atomic concentrations and oxidation states of the elements present in the catalytic samples. Fig. 10 displays the Ce3d core level signal which is comprised of 10 peaks; four of them correspond to Ce^{3+} 3d final states and six of them to Ce^{4+} 3d final states. Mixed Gaussian-Lorentzian functions were used to model these peaks [47]. The main features for Ce^{4+} are located at 883.2eV (v), 889.2eV (v''), 899.5eV (v'''), 901.7eV (u), 908.2eV (u'') and 916.7eV (u''') whereas for Ce^{3+} at 886.2eV (v'), 904.7eV (u'), 881.2(v_0), 899.5eV (u_0). The percentage of Ce^{3+} species (Table 5) was determined from the deconvoluted spectra, as the ratio of the sum of the u0, u', v0, and v' peaks intensity to the whole Ce3d spectra intensity [48-49]. For $NSCeCu_{imp}$ sample, the Ce^{3+} (%) value could not be estimated due to the low resolution. By correlating the obtained Ce^{3+} (%) values with ceria's crystal size derived by XRD analysis, a size dependence of the generated Ce^{3+} fraction can be observed. NSCe and $NSCeCu_L$ samples consisting of the smallest ceria nanocrystals, 2 and 3 nm respectively, possess the highest Ce^{3+} content. However, the slightly highest Ce^{3+} percentage calculated in $NSCeCu_L$ sample, despite its larger CeO_2 size, signifies that formation and stabilization of Ce^{3+} species is further enhanced upon introduction of copper ions. These findings are consistent with literature data, stressing the beneficial effect of particle size and metal-support interactions on ceria's redox properties [25, 50-51].

In Fig. 11, the Cu $2p_{3/2}$ core level peak is depicted. As documented in the literature, a higher Cu $2p_{3/2}$ binding energy (933.0–933.8 eV) and the appearance of the shake-up peak are both associated with the presence of Cu(II) / CuO species, while a lower Cu $2p_{3/2}$ binding energy (932.2–933.1 eV) and the absence of the shake-up peak are characteristic of reduced copper species [44-46]. On this basis, the broad Cu 2p3/2 signal in $NSCu_{imp}$ and $NSCeCu_H$ catalysts which can be deconvoluted into two peaks

and the shake-up satellite at 938–946 eV point towards the co-existence of CuO with reduced Cu species in these samples. This is further supported by the relative intensity of the satellite with respect to the main line estimated about 0.38 (for both samples), lower than 0.55 corresponding to pure Cu^{2+} [22, 44]. Regarding the reduced copper forms (Cu^{+} or Cu^{0}) an accurate distinction can be attained only by using the information acquired from the Auger spectra, given their similar BE values [44-45]. However, considering that all samples were subjected to thermal treatment under air atmosphere, reduced copper species are more likely in the Cu^{+}/Cu_2O and not in the Cu^{0} form. In $NSCeCu_{imp}$, $NSCeCu_{L}$ and $NSCeCu_{L}$–aged samples (with lower Cu content 2 wt. %), the Cu $2p_{3/2}$ signal consists of one contribution centered at lower binding energy, around 932.8–933 eV, not accompanied by a shake-up peak. These observations indicate the dominance of Cu^{+} either in well-dispersed Cu_xO clusters or in Cu-O-Ce sites [14, 22, 45-46].

The intensities of the core level peaks corrected by the corresponding relative sensitivity factors (RSFs) were used for the quantitative analysis and the calculation of the surface atomic concentrations (Table 5). A marked difference can be observed between the values listed in Table 1, corresponding to bulk quantities determined by UV-vis, and those derived from XPS analysis. In fact, the XPS results revealed much lower Ce/Cu atomic ratios than that in the bulk (Ce:Cu = 1:0.3 for low Cu loadings and Ce:Cu = 1:0.9 for high Cu loadings), implying surface enrichment with copper species. It is worth mentioning that the $NSCeCu_{L}$ Ce/Cu atomic ratio, 2.5 times higher compared to $NSCeCu_{imp}$ sample, suggests a more uniform distribution of ceria and CuO active phases onto the siliceous matrix, in line with TEM and XRD analyses results.

3.9 Activity Tests

The pollutants' conversion profiles as a function of catalyst temperature are illustrated in Fig. 12. In Table 6 the light-off temperatures (temperature required for 50% conversion of each reactant) and maximum conversion values are listed.

Activity towards CO oxidation is depicted in Fig. 12A. Copper oxide – ceria loaded nanoporous samples ($NSCeCu_L$ and $NSCeCu_H$), derived from the direct introduction of cerium and copper ions, exhibit the optimum performance reaching 100 % conversion at 400^oC and very low light-off temperatures at 250^oC and 265^oC respectively. The significant effect of the employed synthetic pathway on the catalytic activity is evident when comparing CO oxidation performances of $NSCeCu_{imp}$ and $NSCeCu_L$ samples, both having the same chemical composition. $NSCeCu_{imp}$ sample produced through sequential impregnation demonstrates inferior behaviour with 94% conversion at 500^oC and 324 ^oC light-off temperature. Catalytic materials comprising of only one active component (CuO or CeO_2), displayed the lowest activity with maximum conversions of 84% at 400^oC and 500^oC and light – off temperatures of the order of 265^oC and 400^oC for $NSCu_{imp}$ and NSCe samples, respectively.

The same trend can be noticed in the other pollutants conversion profiles. In the case of C_3H_6 oxidation the best performance is observed for the $NSCeCu_L$ and $NSCeCu_H$ samples with 100 % conversion at 400 ^oC and approximately the same light-off temperatures of about 295 ^oC. $NSCeCu_{imp}$ sample achieves 97 % conversion at 500 ^oC and light-off temperature around 345 ^oC whereas profiles shifted at significantly higher temperatures (light-off temperatures at 415^oC) were recorded in the case of $NSCu_{imp}$ and NSCe samples with 100 % and 89 % maximum conversions at 500 ^oC respectively.

In Fig. 12C and 12D present the NO and propane (C_3H_8) conversion efficiencies versus temperature. All materials exhibit NO and C_3H_8 conversions lower than 20% and 30 %, respectively. The highest catalytic performance is achieved by the $NSCeCu_L$ catalyst, demonstrating maximum conversions of 14.3% at 300^oC for NO and 29.2% at 500^oC for C_3H_8. In the case of NO conversion profile, a maximum at 300 ^oC is observed followed by a decrease to 5% at higher temperatures (500 ^oC). Finally, all materials were found inactive for methane oxidation, (conversion profiles not shown). This limited oxidation activity is expected considering that methane abatement, in the absence of noble metals, usually requires higher temperatures, whereas the presence of H_2O significantly inhibits this reaction [52-53].

Overall, the optimum catalytic performance, for all pollutants, is exhibited by $NSCeCu_L$. Driven by its notable oxidation activity additional catalytic tests were performed by employing fuel-rich and fuel-lean mixtures. The acquired conversion profiles depicted in Fig. 13, show high oxidation activities remaining under fuel rich environment. Although light-off temperatures are slightly increased, 50 ^oC for CO and 25 ^oC for C_3H_6, total CO and C_3H_6 conversions are achieved at approximately the same temperatures, in relation to those recorded at the stoichiometric point. Interestingly, C_3H_8 conversion is enhanced under fuel rich conditions, with 38 % maximum conversion reached at 500 ^oC compared to 29 % and 25 % under stoic and lean conditions respectively. Finally, as expected, a marked improvement was observed towards NO conversion, from 14 % to 60 % at 500 ^oC. The retained or even superior oxidation activity observed under fuel rich mixtures could be mainly attributed to ceria's redox properties and thus its oxygen buffer capacity. Fuel lean environment, on the other hand, induced a slight increase in C_3H_6 conversion and a negligible deterioration in NO activity.

Further investigation of this material in terms of thermal stability included additional heat treatment at elevated temperature (800 ^{o}C for 5 hrs) in an oxidative atmosphere and subsequent activity measurements at the stoichiometric point. As inspected from the catalytic results plotted in Figs. 12A-D, thermal aging led to a deterioration of the catalytic behaviour, mirrored in the shifting of the conversion profiles to higher temperatures and the slightly lower maximum conversion values. However, this sample still exhibited significant efficiency in CO and C_3H_6 oxidation (90-100 %). For the rest of the pollutants the observed changes are not significant, probably due to the low conversions achieved.

The two factors exerting the most pronounced effect on the catalytic performance are the presence of CuO and CeO_2 components into the nanoporous silica network and the employed synthetic pathway. As shown, CuO and CeO_2 are both active phases for CO and HC oxidation reactions; however their co-existence in the catalytic system results in a substantial improvement of the catalytic performance, 110-150^{o}C lower light-off temperatures and 100 % conversion at 400 ^{o}C. This synergistic effect between copper and ceria, also substantiated by TRP and XPS measurements, is well documented in the literature and ascribed to Ce^{4+}/Ce^{3+} and Cu^{2+}/Cu^{1+} redox pairs' interplay, promoting the reducibility of CuO and oxygen storage capacity (OSC) of CeO_2 [14-15, 17, 19-22, 24-26, 28-29, 54]. Therefore, interaction between CuO and CeO_2 initiates a co-operative effect which is considered responsible for the increased catalytic activity.

Regarding the synthesis route, direct introduction of Ce(III) & Cu(II) into the initial reaction mixture (one-step synthesis) produces materials with superior physicochemical properties according to N_2 adsorption, XRD, TEM, TPR and XPS analyses. $NSCeCu_L$ sample possesses larger surface area and pore volume values,

smaller sized ceria crystallites and an excellent dispersion of Cu species compared to $NSCeCu_{imp}$ sample. As a consequence of higher homogeneity and smaller nanosized CuO and CeO_2 particles present in $NSCeCu_L$ sample, the possibility of active components being in close proximity is increased. This intimate contact between CuO and CeO_2 species, generating a larger number of highly active Cu-O-Ce interfacial sites, is confirmed by the enhanced reducibility and the larger Ce^{3+} fraction revealed by TPR and XPS studies, fully justifying the superior oxidation performance and pointing out the effectiveness of one-step synthesis in producing composite nanoporous catalysts.

Furthermore, $NSCeCu_L$, produced through the one-step synthetic pathway exhibits significant thermal stability, withstanding exposure at elevated temperatures, up to 800 ^oC, in oxidative atmosphere. TEM, XRD and N_2 adsorption analyses revealed that after thermal treatment it retains its unique porous architecture. Despite the deterioration in pore structural characteristics (≈ 30 %) no evident CuO or CeO_2 agglomeration and grain growth phenomena were induced since no CuO X-ray signals or increase of ceria's particle size could be detected from the wide angle XRD and TEM analyses. The active components' effective stabilization in a highly dispersed state inhibits undesirable sintering phenomena and results in a thermally stable catalytic material.

Copper loading, on the other hand, did not have a monotonic effect on catalytic performance. This behavior could be attributed to the poorer textural characteristics of $NSCeCu_H$ in comparison with $NSCeCu_L$ sample (ssa of 365 m^2/g *vs* 679 m^2/g) and to the chemical nature of copper species present in the catalytic systems. As already mentioned at high copper loadings formation of larger CuO crystallites was favoured (average size around 25 nm), as determined by TEM microscopy, XRD, TPR and

XPS analyses. However, as it is well-recognised, only the presence of highly dispersed CuO clusters or CuO species associated with ceria is beneficial to catalytic activity [16-17, 24]. Therefore, in $NSCeCu_H$ sample (6.5 % wt Cu loading) the excess of CuO species resulted in the formation of bulk CuO particles upon calcination and did not contribute to the overall catalytic performance.

This work entails a preliminary investigation of the newly developed composite oxides revealing their potential use in automotive catalysis. Ongoing studies will be focussed on a more detailed evaluation of the positive role of the siliceous porous framework and of the effect of higher calcination temperature to CuO - CeO_2 interaction. Additionally, more samples with different active phases and loadings will be produced anticipating further optimization of the catalytic performance.

4. Conclusions

The described hyperbranched polymer templating method enables the development of CuO-CeO_2-SiO_2 nanoporous materials that could constitute an essential component in automotive aftertreatment systems. Catalytic tests under harsh and realistic operational environment reveal very high oxidation activity, especially towards CO and C_3H_6, in all conditions investigated and efficient NO removal when a fuel-rich mixture is employed. The enhanced performance could be attributed to the highly porous wormhole-like network and uniform distribution of CuO and CeO_2 nanocrystallites into the amorphous silica matrix. The large surface areas and pore volume values (up to 679 m^2/g and 0.42 cm^3/g) facilitate diffusion and accessibility of reactant gas molecules to the catalytic active sites. Additionally, the fine dispersion of ceria and copper oxide species affords an increased population of nanosized particles and highly reactive Cu-O-Ce sites, as shown by TPR and XPS studies. The intriguing

structural and textural features of the produced materials emanate from hyperbranched polyethyleneimine's chemical and chelating properties. PEI possesses a dual role; it regulates the porous structure of the silica framework and immobilizes guest species through complex formation, as evidenced by N_2 adsorption and UV-Vis spectroscopy. Three-way catalytic performance was found to be strongly correlated to the adopted synthetic pathway. Direct introduction of Ce(III) and Cu(II) into the initial reaction mixture (one-step synthesis) generates more homogeneous materials with increased porosity, superior catalytic activity and notable thermal stability. This versatile procedure, is not necessarily limited to the metal ions used in this work but could also be employed for the preparation of homogenous composite oxide materials with varying metal species in high dispersion depending on the intended application.

Acknowledgements

Partial financial support from European Union's 7th Framework Programme under grant agreement No. 280890-NEXT-GEN-CAT is gratefully acknowledged. The authors also thank BASF for the donation of Hyperbranched polyethyleneimines and Dr. Labrini Sygellou for the XPS measurements (Foundation for Research and Technology, Hellas-Institute of Chemical Engineering and High Temperature, P.O. Box 1414, 26504 Patras, Greece).

References

[1] S. Roy, M.S. Hegde, G. Madras, Catalysis for NOx abatement, Appl. Energy 86 (2009) 2283–2297.

[2] M.A. Gomez-Garcia, V. Pitchon, A. Kiennemann, Pollution by nitrogen oxides: An approach to NOx abatement by using sorbing catalytic materials, Environ. Int. 31 (2005) 445– 467.

[3] P. Bielaczyc, J. Woodburn, A. Szczotka, An assessment of regulated emissions and CO_2 emissions from a European light-duty CNG-fueled vehicle in the context of Euro 6 emissions regulations, Appl. Energy 117 (2014) 134–141.

[4] A. Papavasiliou, A. Tsetsekou, V. Matsouka, M. Konsolakis, I.V. Yentekakis, N. Boukos, Development of a Ce–Zr–La modified Pt/γ-Al_2O_3 TWCs' washcoat: Effect of synthesis procedure on catalytic behaviour and thermal durability, Appl. Catal. B: Environm. 90 (2009) 162–174.

[5] A. Papavasiliou, A. Tsetsekou, V. Matsouka, M. Konsolakis, I.V. Yentekakis, An investigation of the role of Zr and La dopants into $Ce_{1-x-y}Zr_xLa_yO_\delta$ enriched γ-Al_2O_3 TWC washcoats, Appl. Catal. A: Gen. 382 (2010) 73–84.

[6] A. Papavasiliou, A. Tsetsekou, V. Matsouka, M. Konsolakis, I.V. Yentekakis, N. Boukos, Synergistic structural and surface promotion of monometallic (Pt) TWCs: Effectiveness and thermal aging tolerance, Appl. Catal. B: Environm. 106 (2011) 228–241.

[7] X. Dong, K. Tsuneyama, T. Hibino, Ultra-low loading Pt–Rh/$Sn_{0.9}In_{0.1}P_2O_7$ three-way catalyst for propane + NO + O_2 reaction, Appl. Catal. B: Environm. 106 (2011) 503– 509.

[8] S. Cai, D. Zhang, L. Shi, J. Xu, L. Zhang, L. Huang, H. Li, J. Zhang, Porous Ni–Mn oxide nanosheets in situ formed on nickel foam as 3D hierarchical monolith de-NOx catalysts, Nanoscale 6 (2014) 7346 – 7353.

[9] G. Larsen, S. Noriega, Dendrimer-mediated formation of Cu–CuO_x nanoparticles on silica and their physical and catalytic characterization, Appl. Catal. A: Gen. 278 (2004) 73–81.

[10] T. Xie, X. Zhao, J. Zhang, L. Shi, D. Zhang, Ni nanoparticles immobilized Ce-modified mesoporous silica via a novel sublimation-deposition strategy for catalytic reforming of methane with carbon dioxide, Int. J Hydrogen Energ. 40 (2015) 9685-9695.

[11] R. Zhang, D. Shi, Y. Zhao, B. Chen, J. Xue, X. Liang, Z. Lei, The reaction of NO + C_3H_6 + O_2 over the mesoporous SBA-15 supported transition metal catalysts, Catal. Today 175 (2011) 26– 33.

[12] X.C. Zheng, S.H. Wu, S.P. Wang, S.R. Wang, S.M. Zhang, W.P. Huang, The preparation and catalytic behavior of copper-cerium oxide catalysts for low-temperature carbon monoxide oxidation, Appl. Catal. A: Gen. 283 (2005) 217–223.

[13] Y. Li, Q. Fu, M. Flytzani-Stephanopoulos, Low-temperature water-gas shift reaction over Cu- and Ni-loaded cerium oxide catalysts, Appl. Catal. B: Environm. 27 (2000) 179–191.

[14] E. Moretti, M. Lenarda, L. Storaro, A. Talon, R. Frattini, S. Polizzi, E. Rodrıguez-Castellon, A. Jimenez-Lopez, Catalytic purification of hydrogen streams by PROX on Cu supported on an organized mesoporous ceria-modified alumina, Appl. Catal. B: Environm. 72 (2007) 149–156.

[15] Q. Liang, X. Wu, D. Weng, Z. Lu, Selective oxidation of soot over Cu doped ceria/ceria–zirconia catalysts, Catal. Commun. 9 (2008) 202–206.

[16] I. Heo, M.H. Wiebenga, J. R. Gaudet, I.S. Nam, W. Li, C. H. Kim, Ultra low temperature CO and HC oxidation over Cu-based mixed oxides for future automotive applications, Appl. Catal. B: Environm. 160–161 (2014) 365–373.

[17] S. Zeng, Y. Wang, S. Ding, J.J.H.B. Sattler, E. Borodina,L. Zhang, B.M. Weckhuysen, H. Su, Active sites over CuO/CeO_2 and inverse CeO_2/CuO catalysts for preferential CO oxidation, J. Power Sources 256 (2014) 301–311.

[18] J. Paier, C. Penschke, J. Sauer, Oxygen Defects and Surface Chemistry of Ceria: Quantum Chemical Studies Compared to Experiment, Chem. Rev. 113 (2013) 3949–3985.

[19] F. Marino, C. Descorme, D. Duprez, Supported base metal catalysts for the preferential oxidation of carbon monoxide in the presence of excess hydrogen (PROX), Appl. Catal. B: Environm. 58 (2005) 175–183.

[20] B. Dou, G. Lv, C. Wang, Q. Hao, K. Hui, Cerium doped copper/ZSM-5 catalysts used for the selective catalytic reduction of nitrogen oxide with ammonia, Chem. Eng. J. 270 (2015) 549–556.

[21] X. Xi, S. Ma, J.-F. Chen, Y. Zhang, Promotional effects of Ce, Mn and Fe oxides on CuO/SiO_2 catalysts for CO oxidation, Chem. Eng. J. 2 (2014) 1011–1017.

[22] E. Moretti, M. Lenarda, L. Storaro, A. Talon, T. Montanari, G. Busca, E. Rodrıguez-Castellon, A. Jimenez-Lopez, M. Turco, G. Bagnasco, R. Frattini, One-step synthesis of a structurally organized mesoporous $CuO\text{-}CeO_2\text{-}Al_2O_3$ system for the preferential CO oxidation, Appl. Catal. A: Gen. 335 (2008) 46–55.

[23] T. Tsoncheva, A. Gallo, I. Spassova, M. Dimitrov, I. Genova, M. Marelli, M. Khristov, G. Atanasova, D. Kovacheva, V. Dal Santo, Tailored copper nanoparticles in ordered mesoporous KIT-6 silica: Preparation and application as catalysts in

integrated system for NO removal with products of methanol decomposition, Appl. Catal. A: Gen. 464–465 (2013) 243–252.

[24] J.L. Cao, Y. Wang, T.Y. Zhang, S.H. Wu, Z.Y. Yuan, Preparation, characterization and catalytic behavior of nanostructured mesoporous $CuO/Ce_{0.8}Zr_{0.2}O_2$ catalysts for low-temperature CO oxidation, Appl. Catal. B: Environm. 78 (2008) 120–128.

[25] C. Tang, J. Sun, X. Yao, Y. Cao, L. Liu, C. Ge, F. Gao, L Dong, Efficient fabrication of active $CuO\text{-}CeO_2$/SBA-15 catalysts for preferential oxidation of CO by solid state impregnation, Appl. Catal. B: Environm. 146 (2014) 201–212.

[26] A. Reyes-Carmona, A. Arango-Díaz, E. Moretti, A. Talon, L. Storaro, M. Lenarda, A. Jiménez-López, E. Rodríguez-Castellón, CuO/CeO_2 supported on Zr doped SBA-15 as catalysts for preferential CO oxidation (CO-PROX), J. Power Sources 196 (2011) 4382–4387.

[27] A. Patel, P. Shukla, T.E. Rufford, V. Rudolph, Z. Zhu, Selective catalytic reduction of NO with CO using different metal-oxides incorporated in MCM-41, Chem. Eng. J. 255 (2014) 437–444.

[28] D. Gu, C.J. Jia, H. Bongard, B. Spliethoff, C. Weidenthaler, W. Schmidt, F. Schüth, Ordered mesoporous Cu–Ce–O catalysts for CO preferential oxidation in H_2-rich gases: Influence of copper content and pretreatment conditions, Appl. Catal. B: Environm. 152–153 (2014) 11–18.

[29] M. Zabilskiy, B. Erjavec, P. Djinović, A. Pintar, Ordered mesoporous CuO–CeO_2 mixed oxides as an effective catalyst for N_2O decomposition, Chem. Eng. J. 254 (2014) 153–162.

[30] A. Jha, D.-W. Jeong, W.-J. Jang, C.V. Rode, H.-S. Roh, Mesoporous NiCu–CeO_2 oxide catalysts for high-temperature water–gas shift reaction, RSC Adv. 5 (2015) 1430-1437.

[31] S. Cai, D. Zhang, L. Zhang, L. Huang, H. Li, R. Gao, L. Shi, J. Zhang, Comparative study of 3D ordered macroporous $Ce_{0.75}Zr_{0.2}M_{0.05}O_{2-\delta}$ (M = Fe, Cu, Mn, Co) for selective catalytic reduction of NO with NH_3, Catal. Sci. Technol. 4 (2014) 93-101.

[32] D. Tsiourvas, A. Tsetsekou, A. Papavasiliou, M. Arkas, N. Boukos, A novel hybrid sol–gel method for the synthesis of highly porous silica employing hyperbranched poly(ethyleneimine) as a reactive template, Microporous Mesoporous Mater. 175 (2013) 59–66.

[33] B. L. Rivas, K.E. Geckeler, Synthesis and metal complexation of poly(ethyleneimine) and derivatives, Adv. Polym. Sci. 102 (1992) 170–188.

[34] H. Thiele, K.H. Gronau, Kupfer- und Nickelkomplexe von Polyäthylenimin, Makromol. Chem. 59 (1963) 207–221.

[35] A. von Zelewsky, L. Barbosa, C.W. Schlapfer, Poly(ethylenimines) as Bronsted metal ions bases and as ligands for metal ions, Coord. Chem. Rev. 123 (1993) 229–246.

[36] T.D. Perrine, W.R. Landis, Analysis of Polyethylenimine by Spectrophotometry of Its Copper Chelate, J. Polym. Sci. Part A-1, 5 (1967) 1993–2003.

[37] N.K. Dutt K. Nag, Chemistry of lanthanons—XVII: Bis-salicylaldehyde ethylenediamine and bis-salicylaldehyde o-phenylenediamine complexes of rare-earths, J. Inorg. Nucl. Chem. 30 (1968) 2493–2499.

[38] J.H. Forsberg, C. Anthony Wathen, The synthesis and properties of diethylenetriamine chelates of the tripositive lanthanide ions, Inorg. Chem. 10 (1971) 1479–1383.

[39] J. Forsberg, T.M. Kubik, T. Moeller, K. Gucwa, The syntheses and properties of β,β',β''-triaminotriethylamine chelates of the tripositive lanthanide ions, Inorg. Chem. 10 (1971) 2656–2660.

[40] J.H. Forsberg, T. Moeller, Rare earths. LXXX. Thermodynamic stabilities of ethylenediamine chelates of the tripositive lanthanide ions in anhydrous acetonitrile, Inorg. Chem. 8 (1969) 889–892.

[41] R.F. Egerton, Electron Energy Loss Spectroscopy in the Electron Microscope, Plenum Press, New York, 1996.

[42] J.M. Esparza, M.L. Ojeda, A. Campero, G. Hernandez, C. Felipe, M. Asomoza, S. Cordero, I. Kornhauser, F. Rojas, Development and sorption characterization of some model mesoporous and microporous silica adsorbents, J. Mol. Catal. A: Chem. 228 (2005) 97–110.

[43] Z. Huang, F. Cui, J. Xue, J. Zuo, J. Chen, C. Xia, Cu/SiO_2 catalysts prepared by hom- and heterogeneous deposition–precipitation methods: Texture, structure, and catalytic performance in the hydrogenolysis of glycerol to 1,2-propanediol, Catal. Today 183 (2012) 42– 51.

[44] G. Avgouropoulos, T. Ioannides, Selective CO oxidation over CuO-CeO2 catalysts prepared via the urea–nitrate combustion method, Appl. Catal. A: Gen. 244 (2003) 155–167.

[45] W. Liu, M. Flytzani-Stephanopoulos, Total Oxidation of Carbon-Monoxide and Methane over Transition Metal Fluorite Oxide Composite Catalysts. II. Catalyst Characterization and Reaction-Kinetics, J. Catal. 153 (1995) 317–332.

[46] W. Liu, M. Flytzani-Stephanopoulos, Transition metal-promoted oxidation catalysis by fluorite oxides: A study of CO oxidation over Cu-CeO_2, Chem. Eng. J. 64 (1996) 283.

[47] P. Patsalas, S. Logothetidis, L. Sygellou, S. Kennou, Structure-dependent electronic properties of nanocrystalline cerium oxide films, Phys. Rev. B Condens. Matter Mater. Phys., 68 (2003) 351041-3510413.

[48] J. Silvestre-Albero, F. Rodriguez-Reinoso, A. Sepulveda-Escribano, Improved metal-support interaction in Pt/CeO_2–SiO_2 catalysts after zinc addition, J.Catal. 210 (2002) 127–136.

[49] Y. Li, X. Wang, C. Song, Spectroscopic characterization and catalytic activity of Rh supported on CeO_2-modified Al_2O_3 for low-temperature steam reforming of propane, Catal. Today 263 (2016) 22–34.

[50] S. Tsunekawa, T. Fukuda, A. Kasuya, X-ray photoelectron spectroscopy of monodisperse CeO_{2-x} nanoparticles, Surf. Sci. 457 (2000) L437–L440.

[51] C. Deng, B. Li, L. Dong, F. Zhang, M. Fan, G. Jin, J. Gao, L. Gao, F. Zhang, X. Zhou, NO reduction by CO over CuO supported on CeO_2-doped TiO_2: The effect of the amount of a few CeO_2, Phys. Chem. Chem. Phys. 17 (2015) 16092-16109.

[52] A. Amin, A. Abedi, R. Hayes, M. Votsmeier, W. Epling, Methane oxidation hysteresis over Pt/Al_2O_3, Appl. Catal. A: Gen. 478 (2014) 91–97.

[53] Y. Lu, K.A. Michalow, S.K. Matam, A. Winkler, A.E. Maegli, S. Yoon, A. Heel, A. Weidenkaff, D. Ferri, Methane abatement under stoichiometric conditions on perovskite-supported palladium catalysts prepared by flame spray synthesis, Appl. Catal. B: Environm. 144 (2014) 631–643.

[54] P.-Y. Peng, I. Jin, T.C.-K. Yang, C.-M. Huang, Facile preparation of hierarchical CuO–CeO_2/Ni metal foam composite for preferential oxidation of CO in hydrogen-rich gas, Chem. Eng. J. 251 (2014) 228–235.

Figure captions

Fig. 1: A) UV-Vis spectra of PEI (dotted red line), copper nitrate (cyan line) and of PEI-Cu(II) complex (blue line) in DMF; B) Plot of absorbance (640 nm, optical path length 1 mm) of PEI-Cu(II) complex vs. Cu:N molar ratio

Fig. 2: A) UV-Vis spectra of PEI (dotted red line), cerium nitrate (black line) and of PEI-Ce(III) complex (orange line) in DMF; B) Plot of absorbance (350 nm, optical path length 1 mm, dilution 1:10) of Ce(III) complex vs. Ce:N molar ratio

Fig. 3: Low angle XRD patterns

Fig. 4: Wide angle XRD patterns

Fig. 5: A-B) N_2 adsorption – desorption isotherms and C-D) NLDFT pore size distributions calculated from the desorption branch

Fig. 6: A-B) TEM and HRTEM micrographs of $NSCeCu_L$ sample and C-D) TEM micrographs of $NSCeCu_L$-aged and $NSCeCu_{imp}$ samples

Fig. 7: TEM micrographs of A-B) $NSCeCu_H$ sample and C-D) HRTEM images of a single Ceria and CuO particle showing (111) and (110) lattice fringes respectively

Fig. 8: TEM micrographs of A) $NSCeCu_L$ and B) $NSCeCu_{imp}$ samples and C-D) their corresponding Ce and E-F) Cu elemental maps.

Fig. 9: Temperature programmed reduction (H_2-TPR) profiles

Fig. 10: Ce3d photoelectron profiles of NSCe, $NSCeCu_{imp}$, $NSCeCu_L$ and $NSCeCu_H$ samples

Fig. 11: Cu2p photoelectron profiles of $NSCu_{imp}$, $NSCeCu_{imp}$, $NSCeCu_L$ and $NSCeCu_H$ samples

Fig. 12: Light-off curves of the catalytic samples for CO and HCs oxidation and NO reduction

Fig. 13: Light-off curves of $NSCeCu_L$ sample at lean (λ=1.02), stoichiometric (λ=1) and rich (λ=0.98) conditions

Table 1

Table 1. Coding, chemical composition and synthesis conditions of the as – developed materials

Samples coding	Description	Cu wt %	CeO_2 wt %
NS	Nanoporous SiO_2	—	—
$NSCu_{imp}$	Impregnation with a Cu^{II} solution (two-step)	6.5	—
NSCe	Direct introduction of Ce^{III}(one-step)	—	20
$NSCeCu_{imp}$	Impregnation with a Cu^{II} solution (two-step)	2.2	20
$NSCeCu_L$	Direct introduction of Ce^{III}&Cu^{II}(one-step)	2	20
$NSCeCu_H$	Direct introduction of Ce^{III}&Cu^{II} (one-step)	6.5	20

Table 2. Typical composition of car exhaust gases in lean, stoichiometric and rich ratio (λ=0.98, λ=1, λ=1.02)

	O_2 %	NO ppm	CO %	CH_4 ppm	C_3H_6 ppm	C_3H_8 ppm	CO_2 %	H_2 %	H_2O %
λ=0.98	0.609	1000	0.9	300	600	300	15	0.3	10
λ=1	0.777	1000	0.7	225	450	225	15	0.233	10
λ=1.02	0.935	1000	0.5	150	300	150	15	0.167	10

Table 3

Table 3. Low – angle X-ray diffraction data and particle sizes of CeO_2 and CuO

Samples	2θ (degrees)	Width at half height (degrees)	Coherent d (Å)	CeO_2 Crystallite size[a] (nm)	CuO Crystallite size[b] (nm)
NS	1.74	1.32	51	—	—
$NSCu_{imp}$	1.73	1.06	51	—	28
NSCe	1.86	1.27	47	2	—
$NSCeCu_{imp}$	1.78	0.89	50	5.3	—
$NSCeCu_L$	1.71	0.89	52	3	—
$NSCeCu_H$	1.68	0.78	53	5.7	26
$NSCeCu_L$-aged	1.69	0.85	52	3	—

[a]Calculated from the Scherrer equation according to the [111] diffraction peak of CeO_2.

[b]Calculated from the Scherrer equation according to the [111] diffraction peak of CuO.

Table 4

Table 4. Pore Structural Characteristics of the as – developed materials

Samples coding	Pore characteristics		
	SSA (m^2/g)	TPV (cm^3/g)	Average Pore Diameter (nm)
NS	833	0.4	2
$NSCu_{imp}$	764	0.52	2.7
NSCe	614	0.34	2.2
$NSCeCu_{imp}$	512	0.32	2.5
$NSCeCu_L$	679	0.42	2.5
$NSCeCu_H$	365	0.3	3.3
$NSCeCu_L$-aged	486	0.32	2.6

Table 5

Table 5. Surface Ce/Cu atomic ratios, Ce^{3+} content (%) and I_{sat}/I_{main} determined by XPS.

Samples	**Ce/Cu**	**Ce^{3+} (%)**	**I_{sat}/I_{main}**
$NSCu_{imp}$	0	0	0.36
NSCe	1	39	0
$NSCeCu_{imp}$	1/1.6	—	0
$NSCeCu_{L}$	1/0.72	40	0
$NSCeCu_{H}$	1/0.65	23	0.36
$NSCeCu_{L}$-aged	1/0.33	15	0

Table 6. Activity tests: Light-off temperatures and maximum conversions

		NO	**CO**	**CH4**	**C3H6**	**C3H8**
$NSCu_{imp}$	T_{50} (^{o}C)	-	275	-	419	-
	T_{max}	450	400	-	500	450
	Conv. (%)	6.5	83.6	0	89.1	2.6
NSCe	T_{50} (^{o}C)	-	425	-	412	-
	T_{max}	300	500	500	500	500
	Conv. (%)	4.8	84.2	0.5	100	5.4
$NSCeCu_{imp}$	T_{50} (^{o}C)	-	330	-	347	-
	T_{max}	350	500	500	500	500
	Conv. (%)	10.2	93.5	0.3	97	10.5
$NSCeCu_{L}$	T_{50} (^{o}C)	-	250	-	299	-
	T_{max}	300	400	500	350	500
	Conv. (%)	14.3	100	4	100	29.2
$NSCeCu_{H}$	T_{50} (^{o}C)	-	265	-	295	-
	T_{max}	350	400	500	400	500
	Conv. (%)	8.7	100	0.6	100	7.4
$NSCeCu_{L}$-aged	T_{50} (^{o}C)	-	342	-	328	-
	T_{max}	300	500	500	450	500
	Conv. (%)	10.6	91.9	1.9	100	22

Figure 3

Click here to download high resolution image

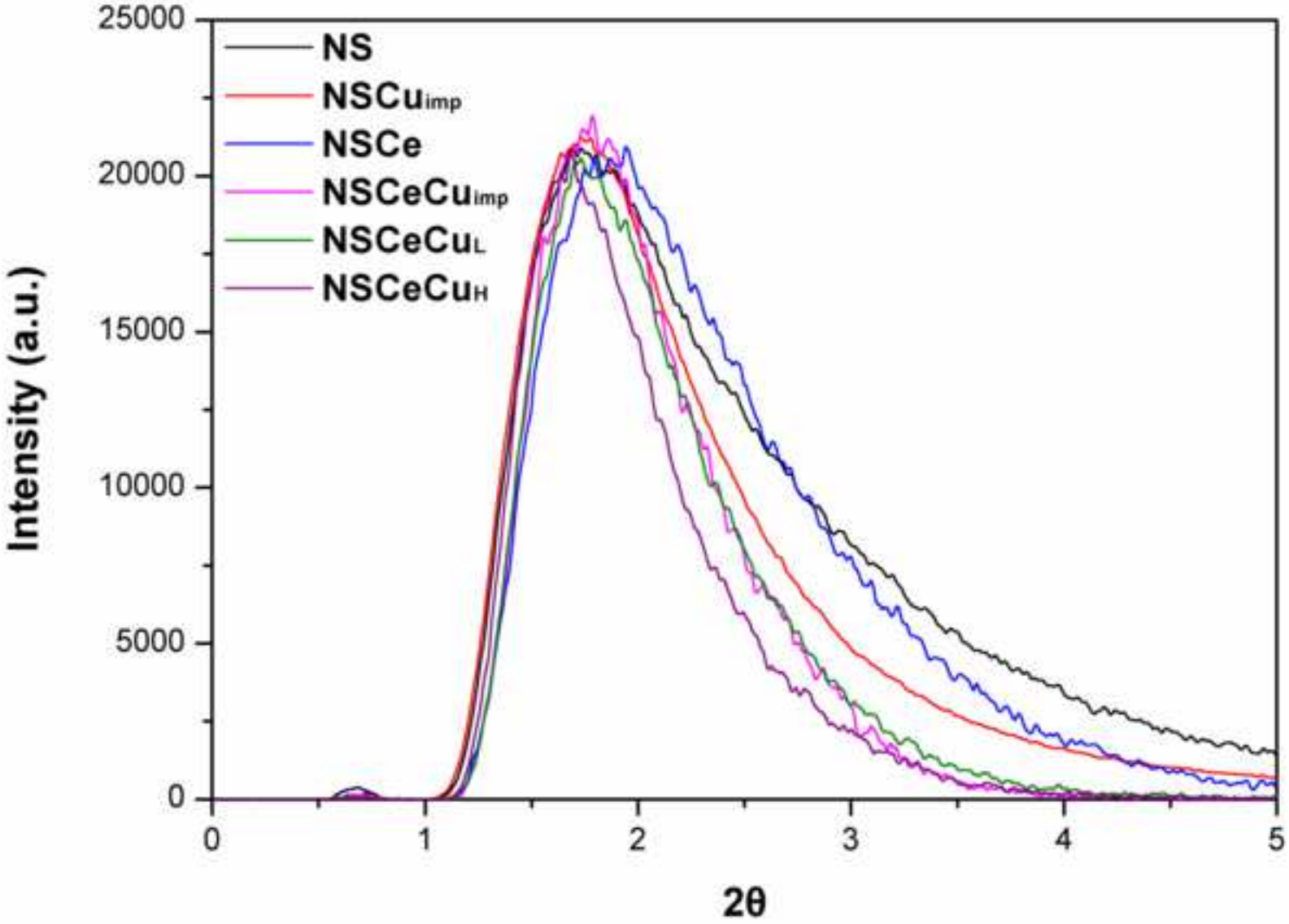

Figure 4

Click here to download high resolution image

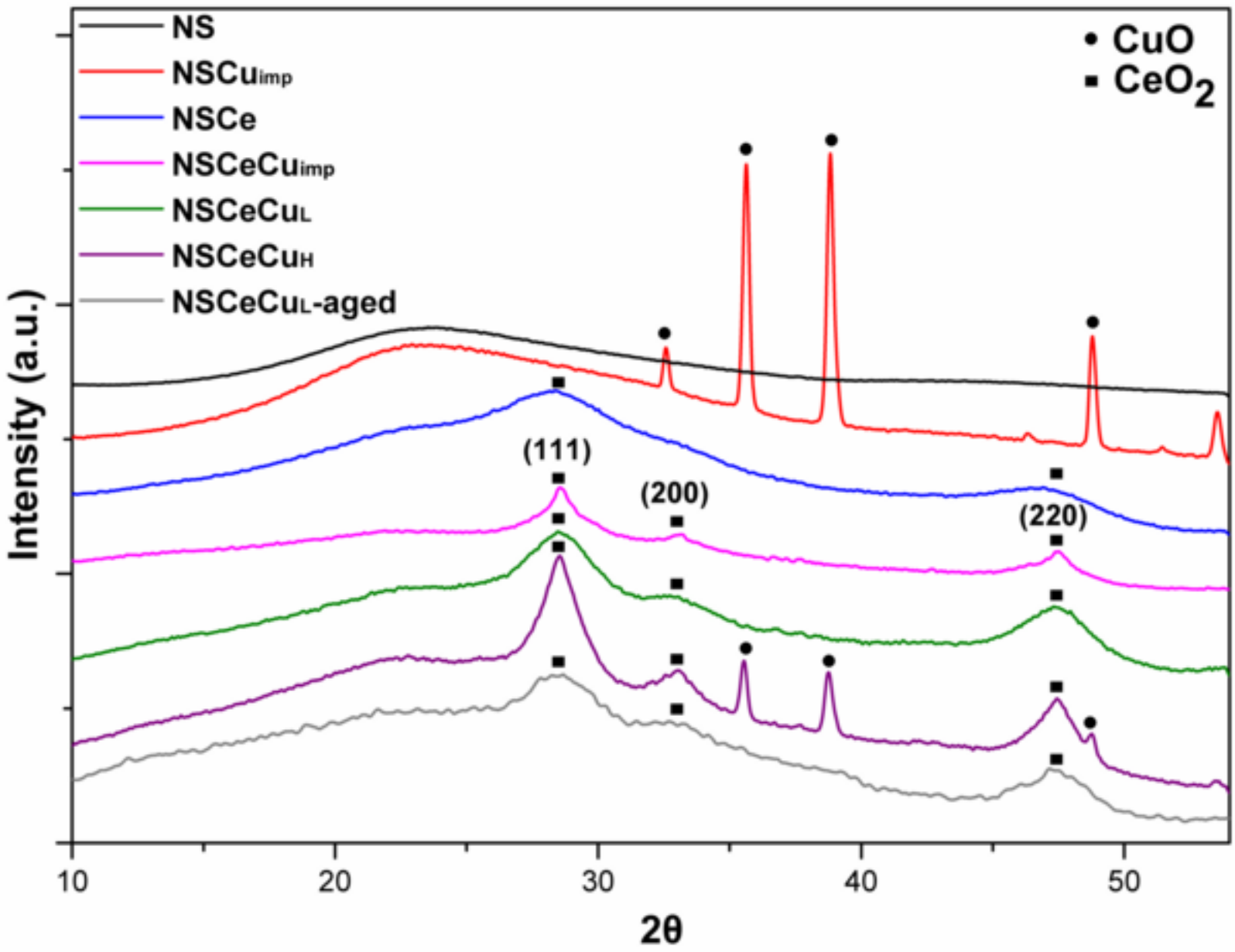

Figure 5

Click here to download high resolution image

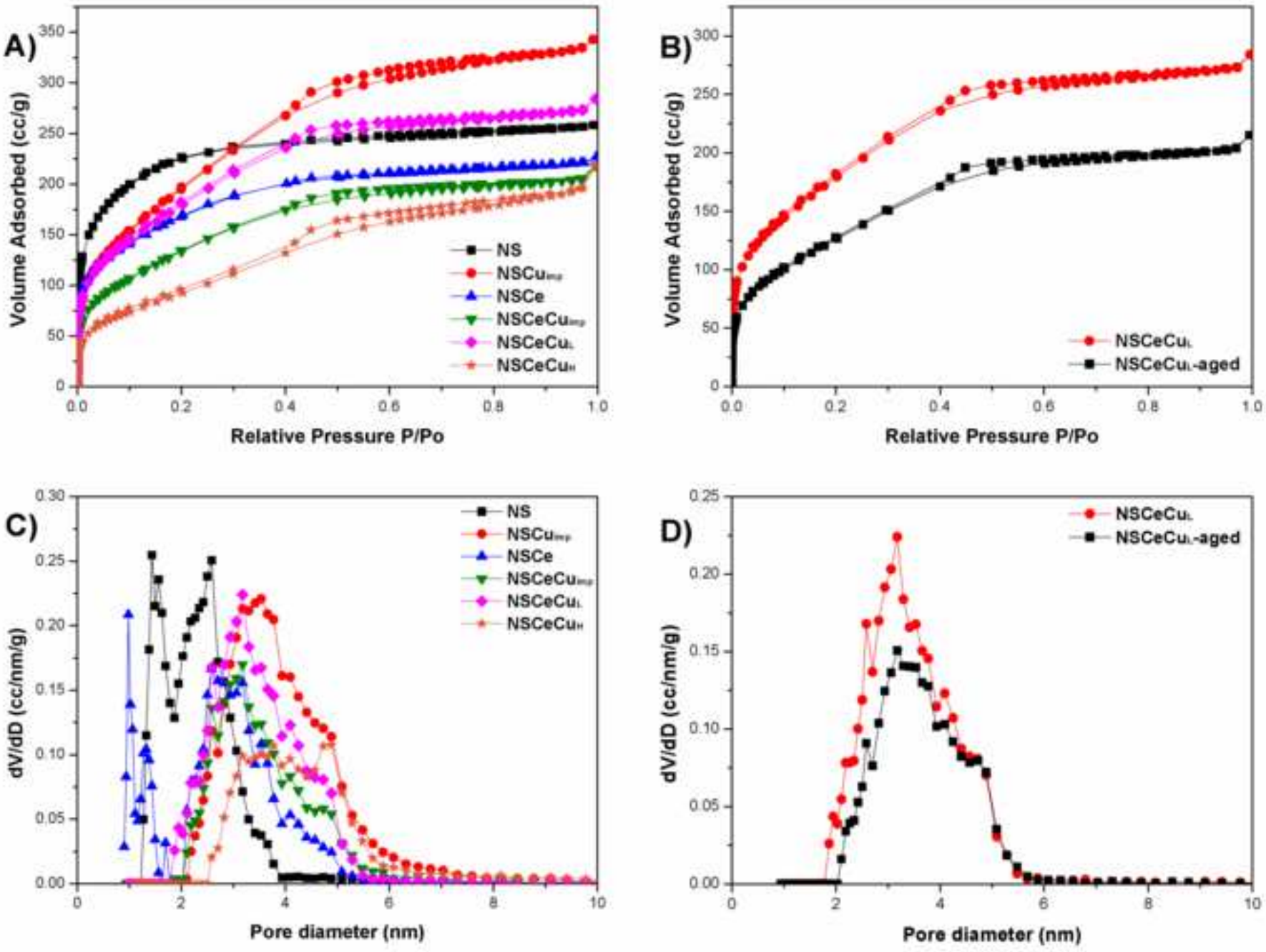

Figure 6

Click here to download high resolution image

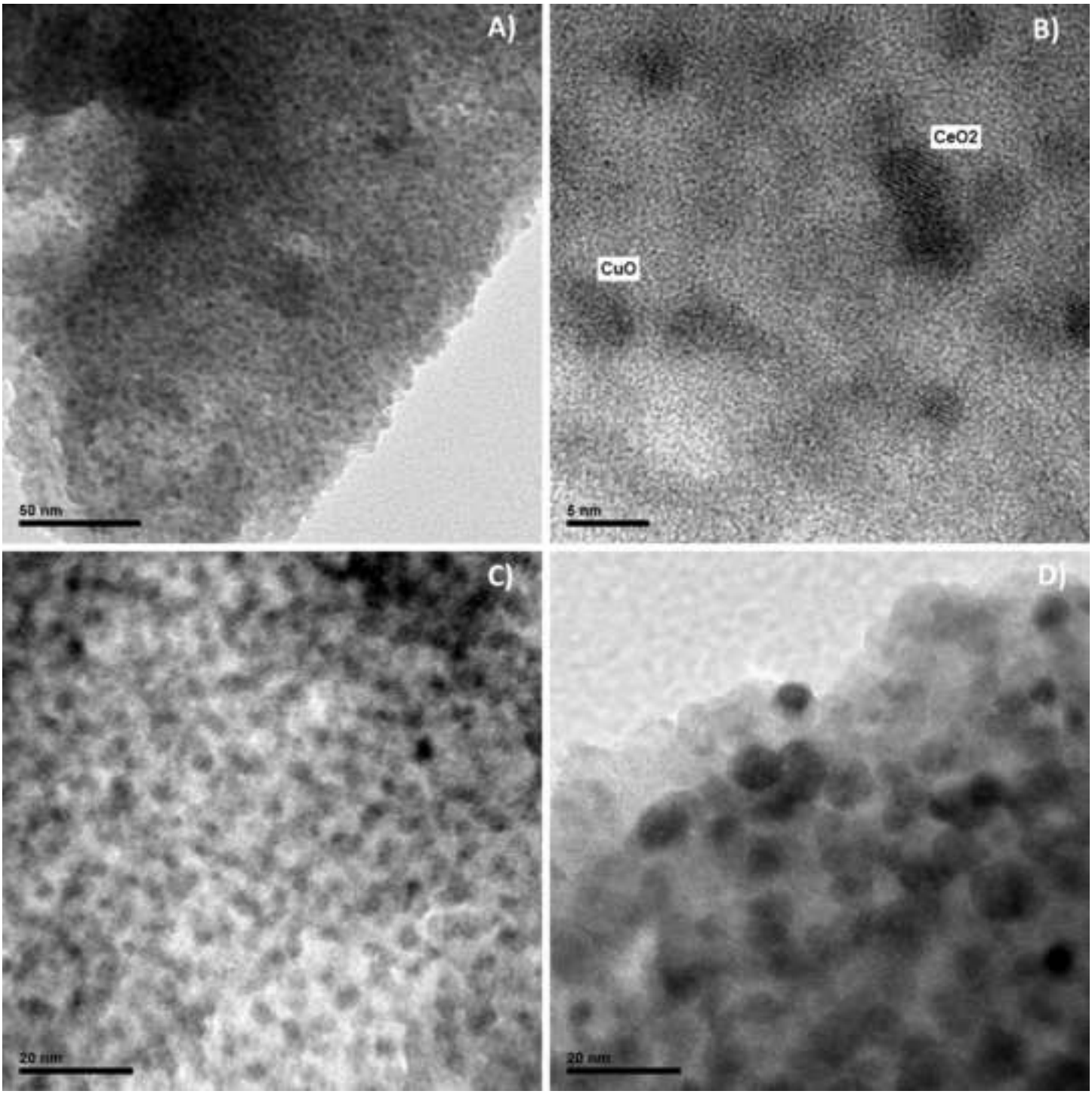

Figure 7

Click here to download high resolution image

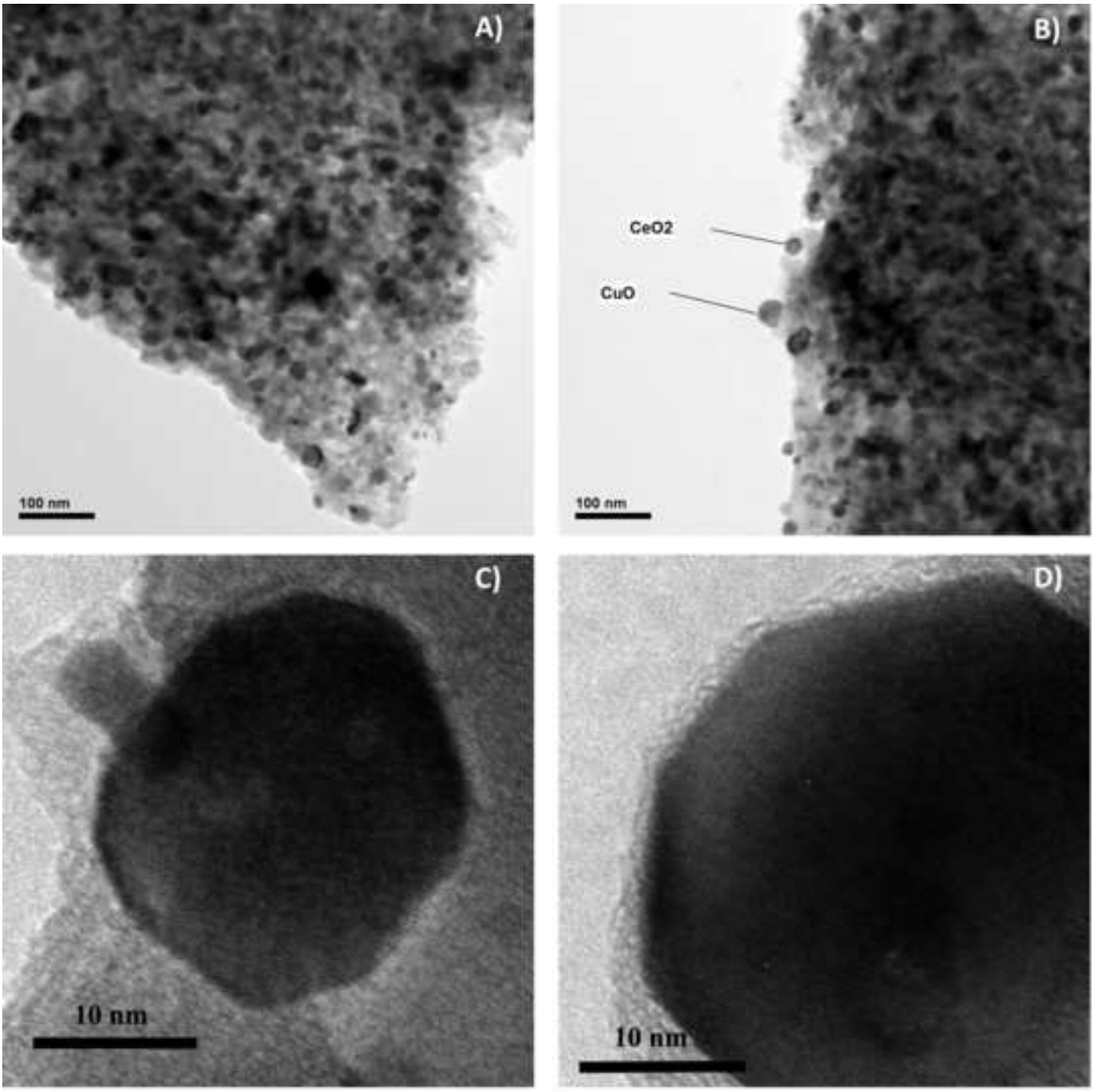

Figure 1

Click here to download high resolution image

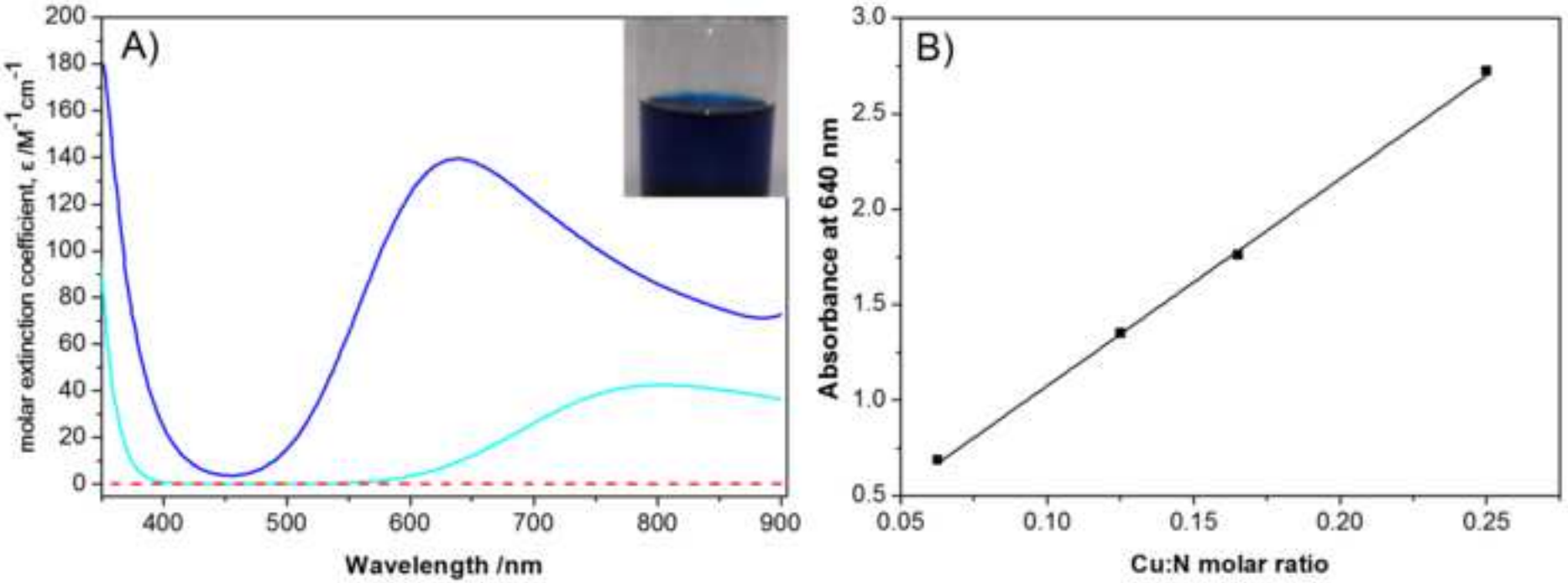

Figure 2

Click here to download high resolution image

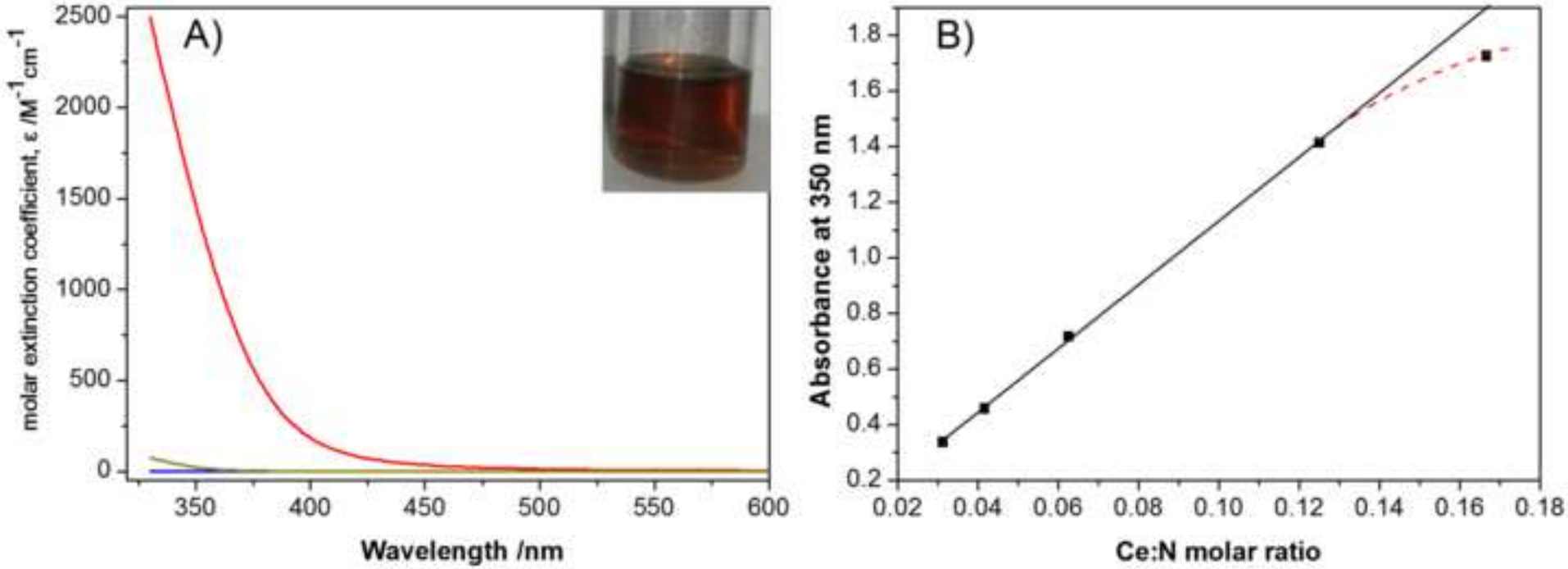

Figure 8

Click here to download high resolution image

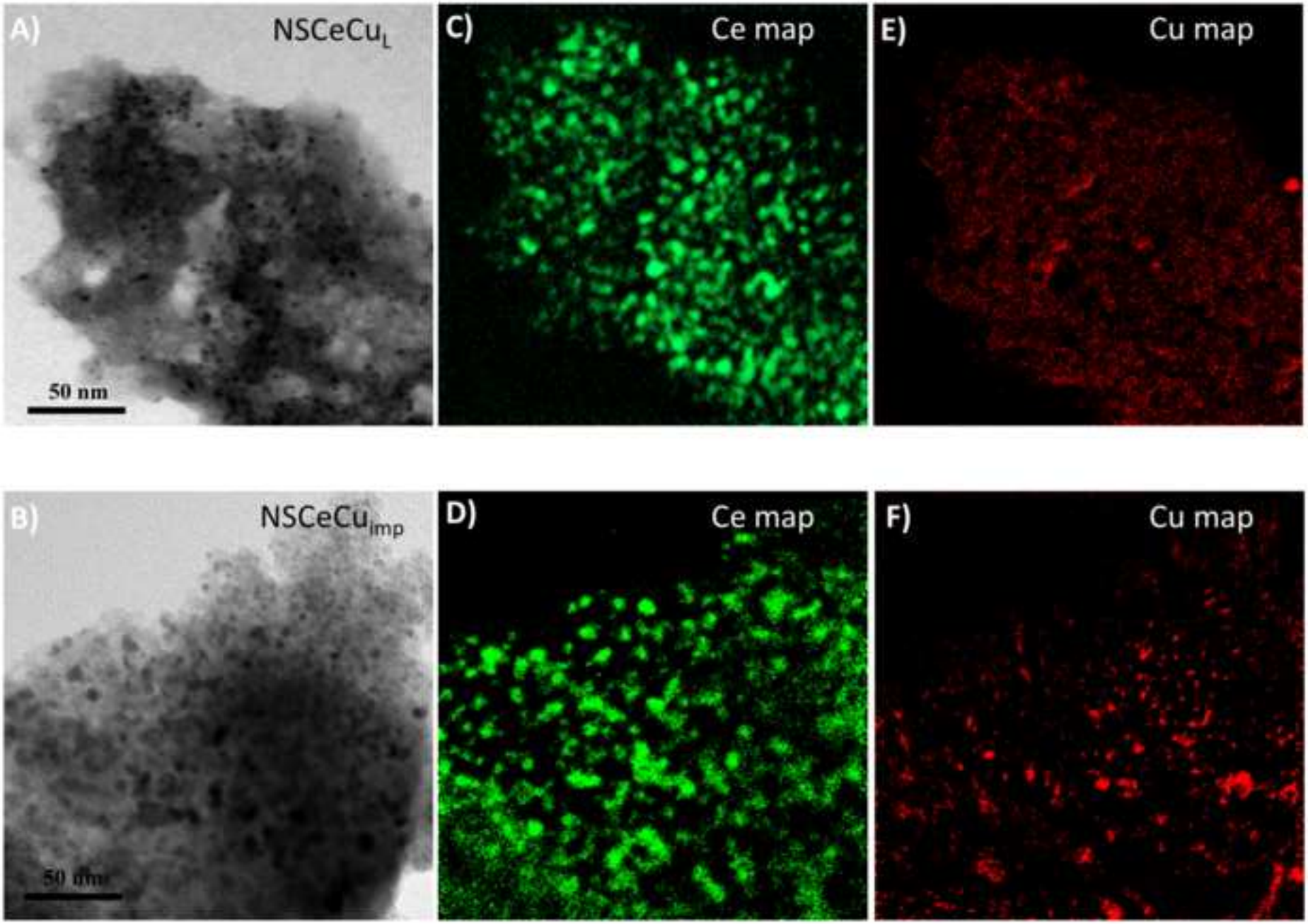

Figure 9

Click here to download high resolution image

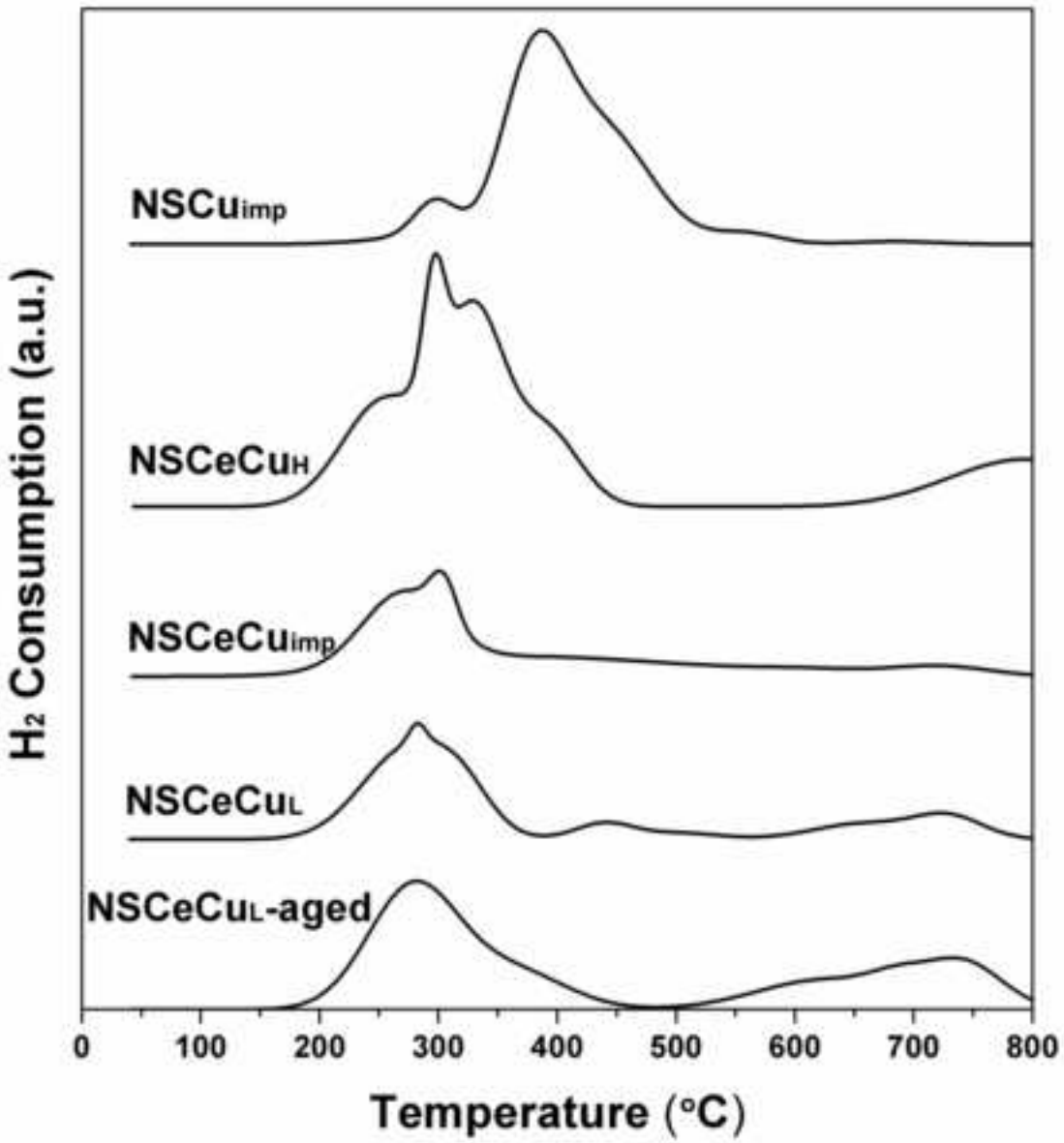

Figure 10

Click here to download high resolution image

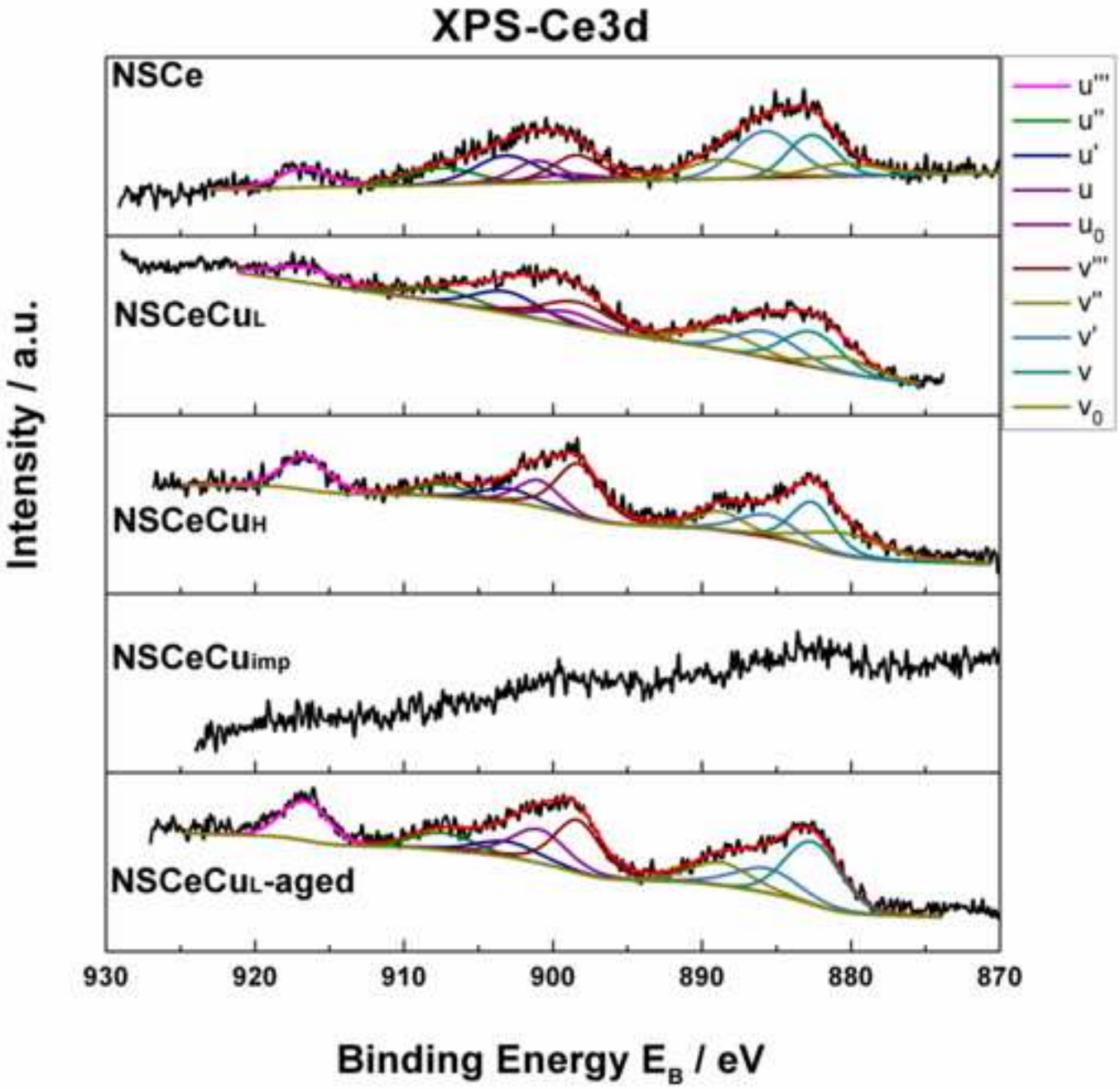

Figure 11

Click here to download high resolution image

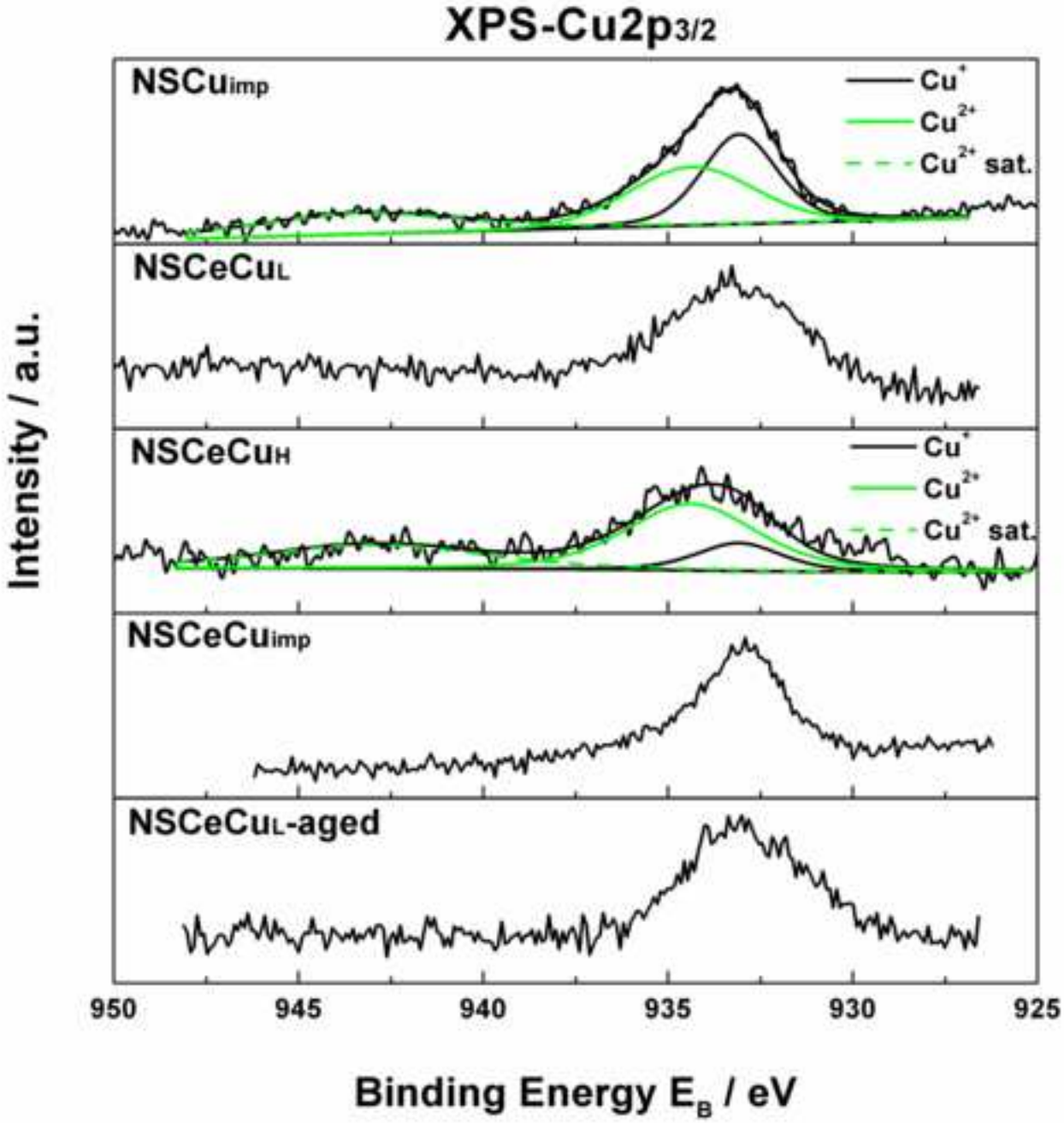

Figure 12

Click here to download high resolution image

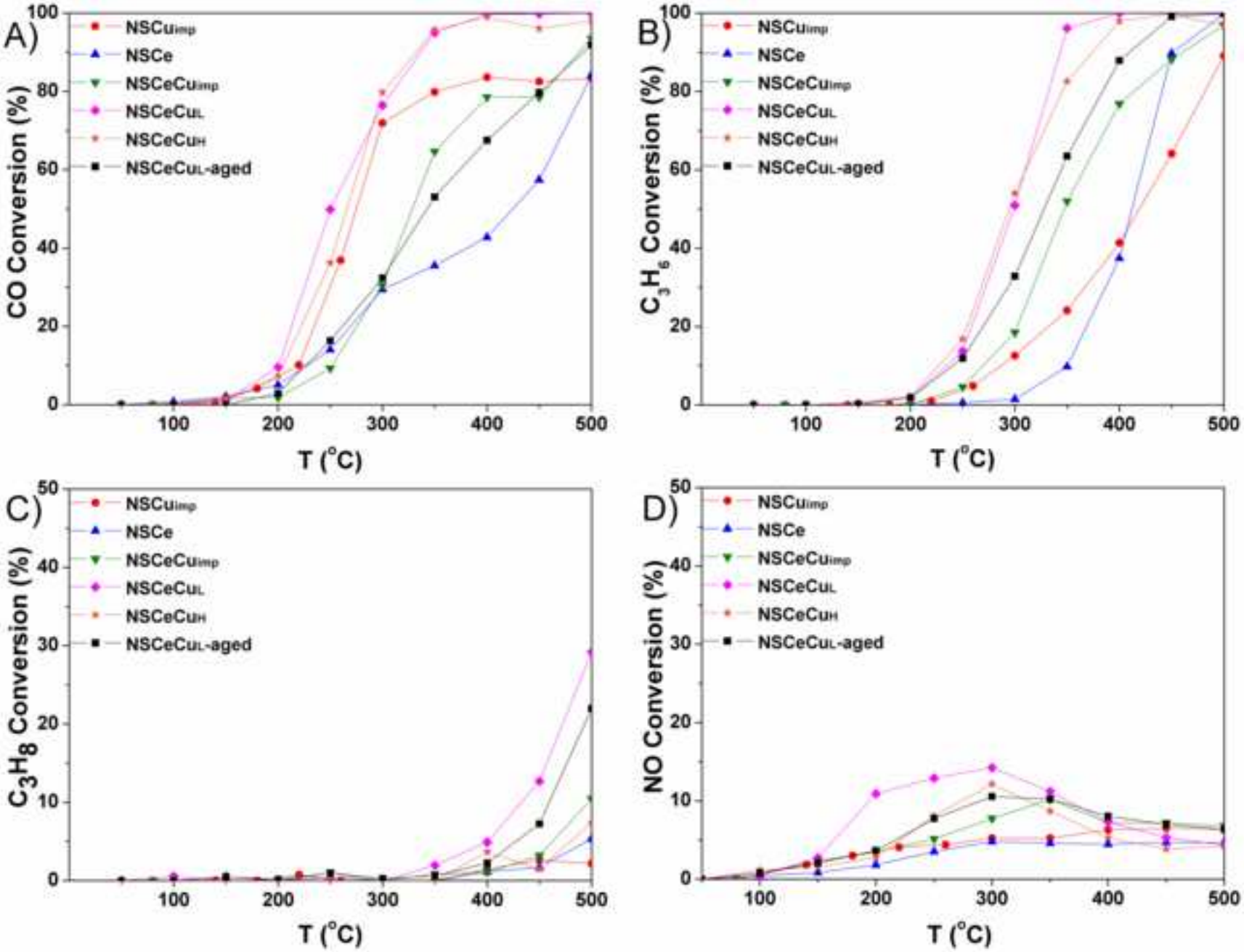

Figure 13

Click here to download high resolution image